Arch Appl Mech (2018) 88:341–372
https://doi.org/10.1007/s00419-017-1312-3

ORIGINAL

H. M. Mobarak · Helen Wu · Joseph P. Spagnol · Keqin Xiao

New crack breathing mechanism under the influence of unbalance force

Received: 29 May 2017 / Accepted: 5 October 2017 / Published online: 16 October 2017

Abstract In this paper, a new analytical model (unbalanced one), which considers the coupling effects of unbalance force, rotor weight, and rotor physical and dimensional properties, is developed to study the actual breathing mechanisms of the transverse fatigue crack in a cracked rotor system. The results are also compared with those of the existing balanced model, where only rotor weight is considered. It has been identified that a crack in the unbalanced model breathes differently from the one in the balanced model. A crack's breathing mechanism in the unbalanced model depends strongly on its location along shaft length. At some special locations, a crack in the unbalanced model may remain fully closed or open during the shaft rotation, which will never occur in a balanced model. It may also behave completely like the one in the balanced shaft. Depending on the crack location, unbalance force magnitude and orientation, the unbalanced shaft may be stiffer or more flexible than the balanced counterpart. It is also demonstrated that the unbalanced model will progressively approach balanced one as unbalance force decreases. Further, different crack breathing mechanisms between two models lead to a large difference along shaft length in the second area moment of inertia, which forms the elements of local stiffness matrix at crack location. It is expected that more accurate prediction of the vibration response of a cracked rotor can be achieved when the effect of unbalance force and rotor properties on the crack breathing has been taken into account.

Keywords Crack breathing mechanism · Crack location effect · Cracked shaft · Unbalance force

List of symbols

φ	Effectual bending angle, bending direction of the shaft relative to the crack direction
δ	Bending direction of the shaft relative to the negative Y-axis
β	The angular position of unbalance force relative to the crack direction
θ	Shaft rotation angle
μ	The ratio of crack depth
η	The ratio of the total weight force to the unbalance force
λ	The ratio of the crack position to the shaft length
Λ	Percentage of opening of the crack
A_1	Area of the uncracked cross section at $t = 0$
$A_2\,(t)$	Area of the closed portion of the crack segment at time t
A_c	Area of the crack segment
F_{un}	Rotational unbalance force

H. M. Mobarak (✉) · H. Wu · J. P. Spagnol · K. Xiao
School of Computing, Engineering and Mathematics, Western Sydney University, Penrith, NSW 2747, Australia
E-mail: mobarak.hossain@westernsydney.edu.au
Tel: +61247360254
Fax: +61247360833

L	Total shaft length
l_0	Location of the crack
l_1	Location of the left disk
l_2	Location of the unbalance force disk
$M_{m_{\mathrm{d}}g}$	Gravitational moment due to two disks
$M_{m_{\mathrm{S}}g}$	Gravitational moment due to shaft self-weight
M_{un}	Dynamic moment due to the rotational unbalance force
M_X	Summation of the moments in X-axis
M_Y	Summation of the moments in Y-axis
M_{R}	Resultant moment
m_{d}	The mass of a disk
$m_{\mathrm{d}}g$	Gravitational force of a disk
m_{s}	Mass of the shaft
$m_{\mathrm{s}}g$	The gravitational force of the shaft
X, Y	Fixed coordinate system
$\bar{X}\bar{Y}$	Centroid coordinate system
$X'Y'$	The rotational coordinate system

1 Introduction

Rotordynamic systems have been widely used in power generation, aircraft engines, compressors, pumps, and many other industrial fields. The extensive use of these rotordynamic systems with continuous heavy loading has the potential for unpredicted failure and damage that may lead to a loss of life and equipment. These damages almost always occur due to propagating fatigue cracks that lead to sudden and destructive vibration scenarios [1]. In rotating machinery, fatigue cracks are considered to be one of the main rotor faults. The breathing of the fatigue crack (when a shaft rotates, the crack opens/closes once per revolution) has a great deal of attention in the literature as one of the main causes of damage in rotor systems [2].

The concept of crack breathing that appears in rotating machinery is the result of the stress and strain distribution around the cracked area that results in the opening and closing of a crack. The stresses and strains acting upon the crack are a result of static loads (self-weight, bearing reaction forces) and dynamic loads (mass unbalance and inertial force) in the form of the bending moment, while the effect of torsion is negligible [3]. When cracks are present in a shaft there is a transient change in flexibility about the crack region corresponding to the breathing of the crack.

Different types of methods for vibration study of a cracked rotor have been reported in the literature, namely model-based method [4–6], signal and vibration-based analysis [7–9], and combined approach [10,11]. A series of numerical and experimental studies were carried out by Andreaus et al. to develop vibration-based crack detection techniques [12–19]. Model-based method plays an important role in the development of online crack detection techniques. This method relies on simplifying the crack breathing mechanism in order to obtain local stiffness matrix of a cracked shaft element and then calculate the vibration response by solving the equations of motion of the system. Early papers [20,21] on cracked shafts used gaping crack model (crack is considered to always be fully open) where the local stiffness of the cracked element is a constant fraction of an uncracked element over a full revolution of the shaft. This stiffness is used to calculate the dynamics of the cracked rotor system [22]. Research using the switching crack model [23–25] depicts the crack as being always fully open in half of a full rotation and always fully closed in the other; however, the sudden change in the stiffness between these two states is not reflective of the true nature of a cracked shaft. Recently, a number of papers [26,27] have used more realistic trigonometric functions to describe the crack breathing mechanism of a rotating shaft.

With the "breathing" mechanism of a crack being known from the simplified analytical model, two important theories were proposed to obtain local stiffness matrix. The first approach is based on the strain energy release rate (SERR) theory [28–30], which is used to calculate the local compliance matrix using approximated stress intensity factor at each point along the crack front. Darpe et al. [31] and Papadopoulos [32] used the SERR approach and calculated the breathing by evaluating on the rectilinear crack tip where the crack is starting to close, assuming that the closed part of the crack surface is delimited by a boundary, the crack closure line (CCL). The same approach was used also by Wu et al. [30]. Bachschmid and Tanzi [33] used 3D finite element method (FEM) to show that, depending on the applied forces, there are no constant strains and stresses along the crack tip. Researchers [34,35] have found that the SERR approach is valid only for the fully

open crack for calculating the additional flexibility due to the crack, but cannot be extended to other crack statuses due to the breathing mechanism.

The second approach is based on a theoretical model of a transverse crack by reducing the area moment of inertia of the element at the location of the crack where this change in area moment of inertia of the cracked shaft is used to develop time-varying stiffness matrix equations. Such a method is seen in [3,26,36–38] and further developed in [39]. Mayes and Davies [40] first demonstrated that a transverse crack in a rotor shaft might be represented by the reduction in the second moment of area of the element at the crack location. They established that the cross section of the rotor shaft at the crack location has asymmetric area moments of inertia about the neutral axis of bending. In Ref. [41] the stiffness matrix due to the transverse crack was obtained at the crack location by using standard finite element method and the opening and closing behavior due to the rotor rotation and shaft self-weight results in a time-dependent stiffness. The authors of [37] implemented the area moment of inertia models in [36,39,42] to perform a parametric stability analysis on cracked Jeffcott rotor using Floquet theory. The finite element method (FEM) was used in modeling the equations of motion of the cracked rotor, where the flexibility matrix was used in modeling the stiffness matrix of the cracked element [43]. The finite element stiffness matrix of a rod in space found in Ref. [44] was used to represent the time-varying stiffness matrix of the cracked element [26,27,41,42,45]. The transfer matrix method was employed in studying the vibration behavior of the cracked rotor system where the second harmonic characteristics are used in detecting the crack in the system [35].

Previous studies based on large rotating machinery have considered the crack breathing mechanism to be dominated by self-weight (weight-dominant breathing). For lightweight rotors, vertical machinery and lightly damped rotors the breathing mechanism is not always weight-dominated as there is significant influence from dynamic loads. Moreover, almost all existing models are not applicable near the shaft critical speed because the lower damping expands the range which dynamic behavior dominates. As such, equations of motion developed under the assumption of rotor weight dominance are no longer suitable for analysis near the critical speed or when the unbalance is high [46–48]. Some studies have considered the effects of significant dynamic loads on the crack breathing mechanism and vibration responses. Previously, the damping of the cracked rotor system was considerably reduced by Bachschmid et al. [3] to study the effect of nonlinear breathing mechanism on the crack in a more severe condition. The hypothesis was developed from the fact that unstable vibration often exhibited the full opening of crack in the breathing behavior. As a result, it was found that stability of the system was restored at times by the presence of this unbalance. In [46], it was also observed that rotor's stability can be restored due to the unbalance. A further proposal was made that the minimum amplitude of vibration is related to the eccentric mass being located at the crack direction and the maximum amplitude of vibration occurs due to the eccentric mass being located to the opposite of the crack. Commercial FEM software was used [49] to simulate a cracked Jeffcott rotor to study the impact of mass unbalance on crack breathing mechanism, highlighting the fact that in the case of some crack depths the crack can be fully closed when the eccentricity is opposite to the crack location. On the other hand, the event of crack and eccentricity being in the same direction causes the crack to remain fully open. In presence of the unbalance it was found the crack breathing behavior greatly differs from the weight-governed crack breathing.

It is evident that an accurate analytical model is still absent, which considers the influence of unbalance force on crack breathing and can be easily used to calculate vibration response numerically. Further, existing analytical crack breathing models were developed under the simple support boundary condition and without considering the rotor physical and dimensional properties. Consequently, crack breathing is independent of crack location. This paper will evaluate the effect of unbalance force, rotor properties and more realistic fixed end boundary condition on the breathing behavior of a fatigue crack. Firstly, the model that describes the relative angle between the crack and bending direction is proposed and visualized for numerous crack location/unbalance configurations. This model, defined in this work as the unbalanced shaft model, is then used to evaluate the nonlinear crack breathing behavior under different weight–unbalance force ratios at different crack locations by examining the percentage of opening of a crack. The results are also validated by Abaqus simulation and compared with those of the balanced shaft model, which neglects the unbalance force.

2 Determination of the effectual bending angle

The opening and closing of a shaft crack are governed by the effectual bending angle φ that describes the proximity of the shaft bending direction (or shaft deformation direction) relative to the crack direction. The model shown in Fig. 1 represents a two-disk rotor supported rigidly by two bearings. It consists of a straight

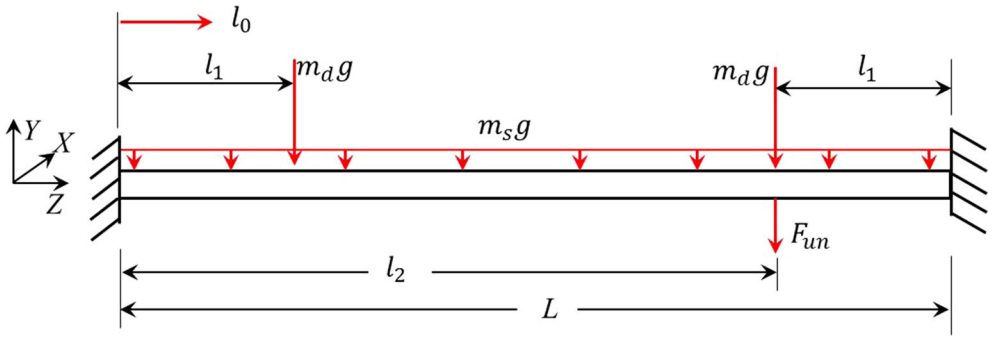

Fig. 1 A two-disk rotor supported rigidly

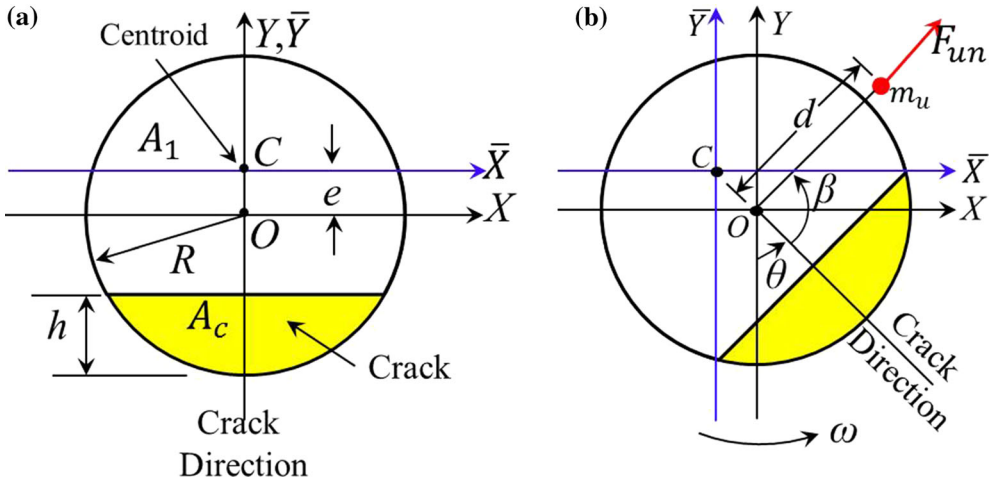

Fig. 2 Schematic diagrams of **a** crack cross section and **b** relative position of unbalance force with respect to the crack

Table 1 Parameters of the chosen rotor system

Description	Value	Description	Value
Shaft length (L)	724 mm	Disk mass (m_d)	0.50 kg
Shaft radius (R)	6.35 mm	Disk-1 location (l_1)	181 mm
Shaft density (ρ)	7800 kg/m^3	Disk-2 location (l_2)	543 mm
Disk outer radius (R_0)	54.50 mm	Crack location (l_0)	Variable
Disk inner radius (R_i)	6.35 mm	Crack depth ratio (μ)	0.5

front oriented crack on a plane normal to the axis of the shaft with non-dimensional crack depth ratio $\mu = \frac{h}{R}$, where h is the crack depth in the radial direction and R is the shaft radius. A_1 is the uncracked cross-sectional area, A_c is the area of the crack segment, and e is the locations of the centroid as shown in Fig. 2a. The unbalance force has been taken as a rotational force $F_{un} = m_u \omega^2 d$ due to an additional mass m_u at a radial distance d from the center of the shaft when the shaft rotates at ω rad/sec. The direction of the rotational unbalance force F_{un} is $(\theta + \beta)$, where θ is the shaft rotation angle and β is a fixed angular position relative to the crack direction as shown in Fig. 2b and the unbalance force is considered being located on the right side disk (see Fig. 1). The parameters of the rotor model are given in Table 1.

Evenly distributed shaft self-weight $m_s g$ will generate a moment along the shaft, where m_s is the mass of the shaft and its vector aligns along the X-axis. The value of this moment at a location l_0 along the shaft length or Z-axis is described in Eq. (1).

$$M_{msg} = \frac{m_s g}{12L}\left(6Ll_0 - L^2 - 6l_0^2\right). \tag{1}$$

The moment in the X-axis at a location l_0 along the shaft length due to the weight of two disks $2m_d g$ is described in Eq. (2).

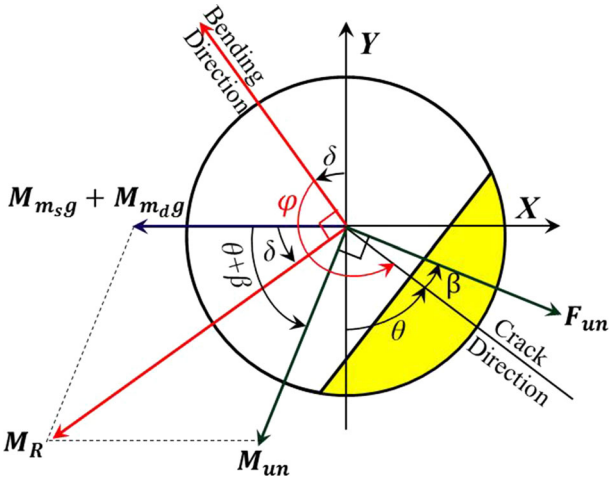

Fig. 3 Definition of the effectual bending angle

$$\left.\begin{aligned} M_{m_{\mathrm{d}}g} &= m_{dg}\left[l_0 - \tfrac{l_1(L-l_1)}{L}\right] && \text{When } l_0 \le l_1 \\ M_{m_{\mathrm{d}}g} &= m_{dg}\left[l_1 - \tfrac{l_1(L-l_1)}{L}\right] && \text{When } l_1 < l_0 < l_2 \\ M_{m_{\mathrm{d}}g} &= m_{dg}\left[(L-l_0) - \tfrac{l_1(L-l_1)}{L}\right] && \text{When } l_0 \ge l_2 \end{aligned}\right\} \tag{2}$$

Correspondingly, the varying moment at a location l_0 along the shaft length due to the unbalance force F_{un} is described in Eq. (3).

$$\left.\begin{aligned} M_{\mathrm{un}} &= F_{\mathrm{un}}\left[\tfrac{l_1^2 l_0}{L^3}(l_1+3l_2) - \tfrac{l_1^2 l_2}{L^2}\right] \\ &= \left(\tfrac{m_{\mathrm{s}}g+2m_{\mathrm{d}}g}{\eta}\right)\left[\tfrac{l_1^2 l_0}{L^3}(l_1+3l_2) - \tfrac{l_1^2 l_2}{L^2}\right] \end{aligned}\right\} \quad \text{When } l_0 \le l_2 \tag{3a}$$

$$\left.\begin{aligned} M_{\mathrm{un}} &= F_{\mathrm{un}}\left[\tfrac{l_2^2 (L-l_0)}{L^3}(3l_1+l_2) - \tfrac{l_1 l_2^2}{L^2}\right] \\ &= \left(\tfrac{m_{\mathrm{s}}g+2m_{\mathrm{d}}g}{\eta}\right)\left[\tfrac{l_2^2 (L-l_0)}{L^3}(3l_1+l_2) - \tfrac{l_1 l_2^2}{L^2}\right] \end{aligned}\right\} \quad \text{When } l_0 > l_2 \tag{3b}$$

where $\eta = \frac{m_{\mathrm{s}}g+2m_{\mathrm{d}}g}{F_{\mathrm{un}}}$ is the ratio of the gravitational force (shaft self-weight, $m_{\mathrm{s}}g$, and two disks' weights, $2m_{\mathrm{d}}g$) to the unbalance force F_{un}.

The gravitational moments $M_{m_{\mathrm{s}}g}$ and $M_{m_{\mathrm{d}}g}$ are constant in magnitude and may change their directions along the X-axis, but always perpendicular to the gravitational forces. The rotational force F_{un} acts in the radial direction $(\theta+\beta)$. Accordingly, M_{un} also rotates in the XY plane and perpendicular to F_{un} (see Fig. 3). According to the principle of superposition theory, the total moment of the system at a location l_0 along the shaft length is described in Eqs. (4) and (5).

$$\text{In } X-\text{axis} \sum M_X = M_{m_{\mathrm{s}}g} + M_{m_{\mathrm{d}}g} + M_{\mathrm{un}}\cos(\theta+\beta) \tag{4}$$

$$\text{In } Y-\text{axis} \sum M_Y = M_{\mathrm{un}}\sin(\theta+\beta)\,. \tag{5}$$

As shown in Fig. 3, shaft bending direction or deformation direction in the crack cross section is always perpendicular to the resultant moment direction. The angle δ of the resultant moment with respect to X-axis is the same as δ of the bending direction with respect to Y-axis. It should be pointed out that unbalance force is not located at the crack plane and F_{un} is only a projection of unbalance force on the crack plane. The effectual bending angle φ is defined as the angle from bending direction to crack direction, and it solely determines

the breathing behavior of the crack. The parameters δ and φ at a crack location are described in Eqs. (6) and (7), respectively; however, modifications were made to ensure these angles are within the co-domain of a full rotation of shaft between 0° and 360°.

$$\delta = \tan^{-1}\left(\frac{\sum M_Y}{\sum M_X}\right) \tag{6}$$

$$\varphi = 180^\circ + \theta - \delta. \tag{7}$$

For the simplicity of the calculations, moments are calculated using simple beam theory [50] with an intact shaft. In the calculations of bending angle as described in Eqs. (6) and (7), the effect of a crack on the moments at the crack cross section in X- and Y-directions are considered to be approximately the same. This assumption will be further examined later by the comparison between analytical and Abaqus results.

3 Determination of breathing mechanism of a crack

Compression and tensile stress field distributions over the cross-sectional area of rotating shafts are determined by the centroid location, neutral axes, and the bending direction. The neutral axis $\bar{X}$ lies perpendicular to the bending direction and passes through the centroid location, C. As the cracked shaft starts to rotate, the locations of the centroid and the neutral axis of the cracked element vary with time. A tensile stress field exists in the $\bar{X}$ and negative $\bar{X}$ plane, and a compressive stress field in the $\bar{Y}$ and positive $\bar{Y}$ (see Fig. 4). A crack is open when the affected part of the material is subjected to tensile stresses and closed when the stress is reversed, which is called the breathing of the fatigue crack.

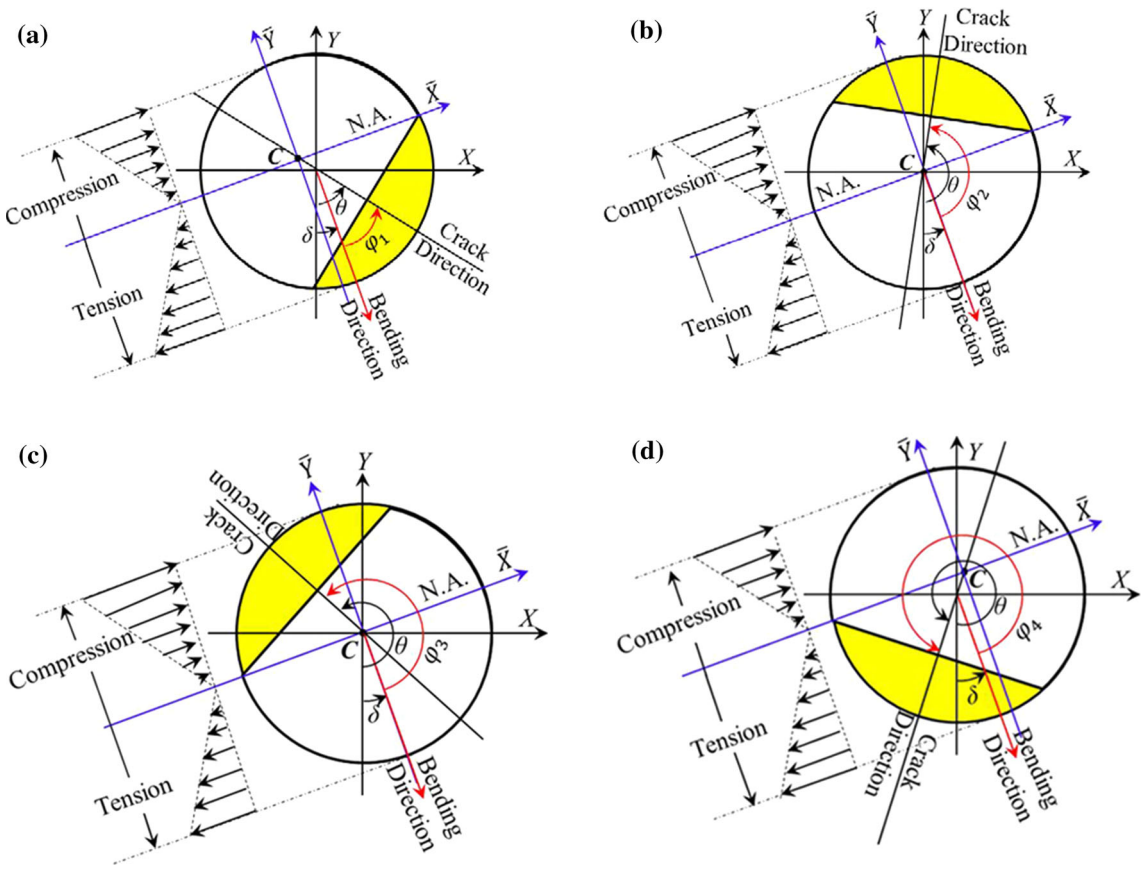

Fig. 4 Key instants of crack breathing in the unbalanced shaft: **a** crack begins to close, **b** right after crack becomes fully closed, **c** crack begins to open and **d** right after crack becomes fully open

The crack starts to close at a certain shaft rotation angle (θ) when the effectual bending angle $\varphi = \varphi_1$, where the upper end of the crack edge reaches the compression stress field as shown in Fig. 4a. The crack becomes fully closed at a certain shaft rotation angle (θ) when effectual bending angle $\varphi = \varphi_2$, where the crack is fully reached in the compression stress field as shown in Fig. 4b. Similarly, the crack starts to open at a certain shaft rotation angle (θ) when effectual bending angle $\varphi = \varphi_3 = 2\pi - \varphi_2$, where the crack edge starts to enter in the tensile stress field as shown in Fig. 4c and then becomes fully open at a certain shaft rotation angle (θ) when effectual bending angle $\varphi = \varphi_4 = 2\pi - \varphi_1$ as shown in Fig. 4d. The intermediate situation between the fully open and fully closed state is partially opened or partially closed status. The effectual bending angles φ_1 and ϕ_2 are a function of cracked shaft geometry as given in Eqs. (8) and (9), respectively, where location of the centroid, e, and uncracked cross-sectional area, A_1, as shown in Fig. 2a are described in Eqs. (10) and (11), respectively.

$$\varphi_1 = \tan^{-1}\left(\frac{e + R\,(1-\mu)}{R\sqrt{\mu\,(2-\mu)}}\right) \tag{8}$$

$$\varphi_2 = \frac{\pi}{2} + \cos^{-1}(1-\mu) \tag{9}$$

$$e = \frac{2R^3}{3A_1}\sqrt[3]{\mu\,(2-\mu)} \tag{10}$$

$$A_1 = R^2\left[\pi - \cos^{-1}(1-\mu) - (1-\mu)\sqrt{\mu\,(2-\mu)}\right]. \tag{11}$$

Equations (8) and (9) were developed by [39] for a balanced shaft. As shown in Fig. 5, the bending direction of a balanced shaft always points toward negative Y-axis and the bending angle is equal to the shaft rotational angle. A crack in the unbalanced shaft has the same opening/closing status as a crack in the balanced shaft as long as they have the same bending angle. The main difference between a balanced shaft and an unbalanced shaft is that the bending direction of the unbalanced shaft keeps changing with the change in shaft rotational angle, unbalance force magnitude and orientation, and crack location. The statuses of the crack at different crack locations during shaft rotation are evaluated quantitatively using percentages of the opening of a crack. The percentage of opening of a crack Λ as described in Eq. (12) is determined using the effectual bending angle by studying the transient change in the area of the cracked cross section. A_c is the area of the crack segment as shown in Fig. 2a, and $A_2(t)$ is the closed portion of the crack segment when effectual bending angle $\varphi_1 \le \varphi \le \varphi_2$ or $(2\pi - \varphi_2) \le \varphi \le (2\pi - \varphi_1)$ (see Fig. 5). A_c can be calculated by Eq. (13) and $A_2(t)$ is determined using a procedure proposed in balanced shaft [39] to calculate the variation of $A_2(t)$ with shaft rotational angle. It is obvious, as shown in Fig. 5, that $A_2(t)$ in the unbalanced shaft is equal to that in a balanced shaft when bending angle in the former is equal to the rotational angle in the latter. For the calculation of $A_2(t)$ in the unbalanced shaft, firstly, $A_2(t)$ for the balanced shaft is calculated using formulas in the above-cited reference paper. This $A_2(t)$ becomes that for the unbalanced shaft at a bending angle equal to the shaft rotational angle in the balanced shaft. Then, using Eqs. 1–7, the $A_2(t)$ with different force ratios at a shaft rotational angle for the unbalanced shaft is obtained. Readers are suggested to consult the original paper for the expressions of $A_2(t)$ for the balanced shaft. For a fully open crack and fully closed crack the percentage of opening of a crack Λ is equal to 100 and 0, respectively.

$$\Lambda\,(\%) = \frac{A_c - A_2(t)}{A_c} \times 100 \tag{12}$$

$$A_c = R^2\cos^{-1}(1-\mu) - R^2(1-\mu)\sqrt{\mu\,(2-\mu)}. \tag{13}$$

4 Results and discussion

The procedure seen in this paper uses the force ratio, η, the ratio of the gravitational force (shaft self-weight and two disks' weights) to the unbalance force, to evaluate the influence of the unbalance force magnitude and the crack location factor, λ, the ratio of the crack position, l_0, to the total shaft length, L, to evaluate the influence of the crack position. The statuses of the crack for different force ratios at different crack locations during shaft rotation are identified using the values of effectual bending angle, φ, relative to the regions formed

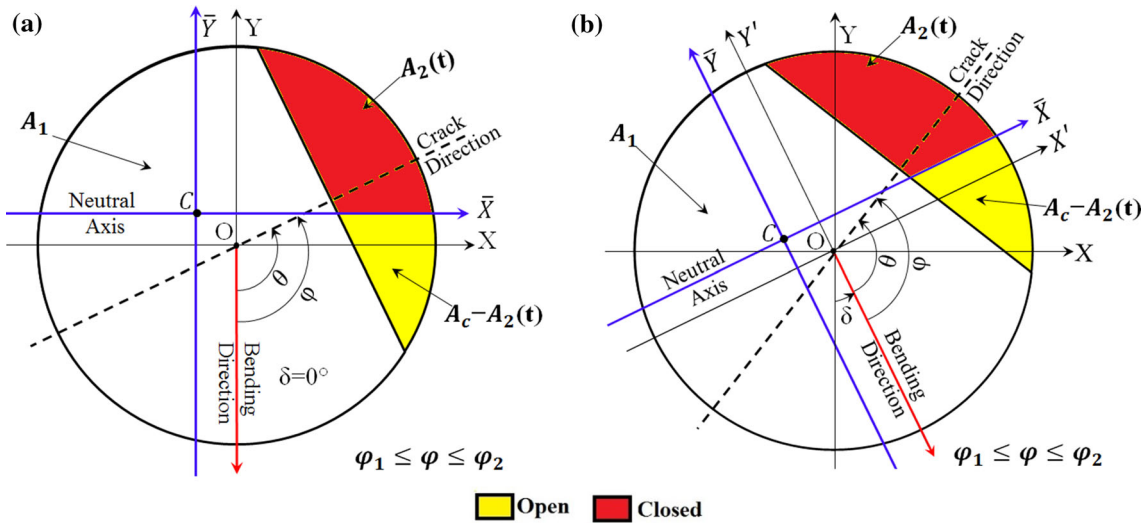

Fig. 5 Schematic diagrams of the closed portion of a breathing crack for **a** a balanced shaft and **b** an unbalanced shaft

by φ_1 and φ_2. A series of analyses have been performed using the MATLAB software. In this analysis the shaft rotation is anticlockwise and the crack initial direction aligns with the negative Y-axis. A crack with a ratio of crack depth $\mu = 0.5$ is chosen to perform the analysis. Throughout the paper a focus is placed on the influences of the unbalance force and crack location on the breathing behavior.

4.1 Effectual bending angle

Figure 6 exemplifies the evolution of the effectual bending angles along the shaft length for different shaft rotation angles and different weight–unbalance force ratios. The effectual bending angles of the balanced shaft are constant, but have a change of 180° at crack locations $\lambda = 0.1946$ and 0.8053, where bending moment due to total gravitational force (shaft and disks) is zero and the moment changes direction across these two inflection points (see Fig. 7). Between two inflection points, the moment is in the positive X-axis and bending direction aligns along the negative Y-axis. Hence, the relation between effectual bending angle and shaft rotation angle is $\varphi = \theta$, which is in agreement with previous result in Ref. [39]. This relation is clearly explained in the example shown in Fig. 7. For the two remaining crack regions the relationship between effectual bending angle and shaft rotation angle is $\varphi = 180° + \theta$.

For an unbalanced shaft, the effectual bending angles along the shaft length are remarkably different from the balanced one. A few findings can be summarized as follows:

(a) There are two shaft rotational angles where the variation pattern of φ along shaft length is similar to the balanced shaft (see Fig. 6a, e). At $\theta = 0°$, the unbalance force is in the same direction as the gravitational force of the rotor, and at $\theta = 180°$ the unbalance force is in the opposite direction to the gravitational force. Furthermore, the locations of zero points of combined moments due to the gravitational force and unbalance force change only slightly at the former shaft rotational angle, but dramatically at the latter angle.

(b) There are two pairs of crack locations along the shaft where the bending angle is independent of the force ratio η. As mentioned earlier at inflection points $\lambda = 0.1946$ and 0.8053, the gravitational moment is zero (see Fig. 7); therefore, the deformation direction or bending direction is solely determined by the unbalance force moment. It should be pointed out that two crack locations are in different unbalance force moment regions, i.e., it is negative at the first location and positive at the second location, as shown in Fig. 8. As a result, the effectual bending angle is 180° at the former crack location and 0° at the latter crack location. Further, as shown in Fig. 6, bending angles at these two locations are independent of not only the force ratio, but also the shaft rotational angle. A small amount of unbalance force would have the same effect on the bending angle as large unbalance force. Therefore, if the crack is located around these two positions then the effect of unbalance force on the crack breathing behavior must be considered. It

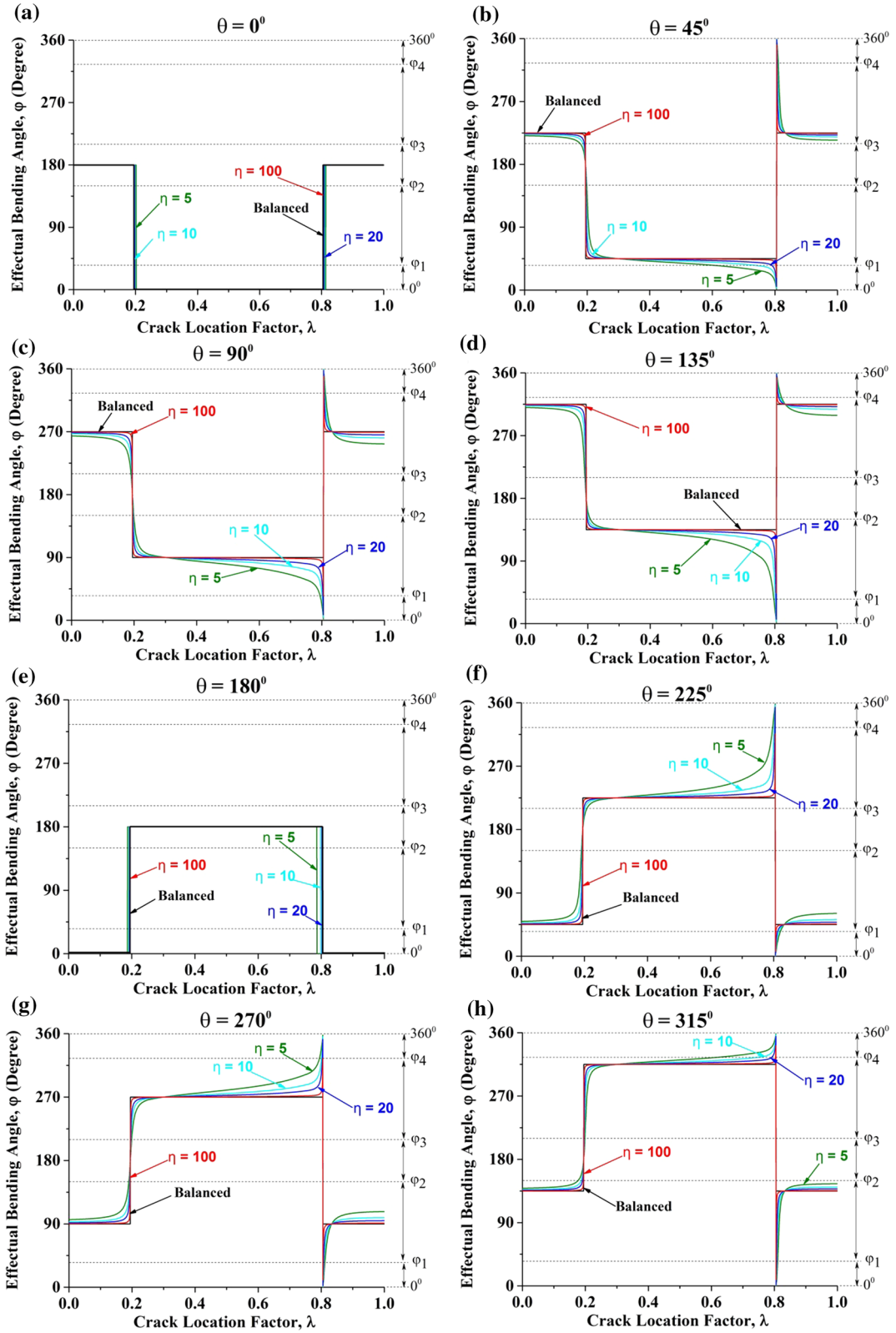

Fig. 6 Effectual bending angles along the shaft length for different shaft rotation angles, θ, with different weight–unbalance force ratios, η, where $\beta = 0°$

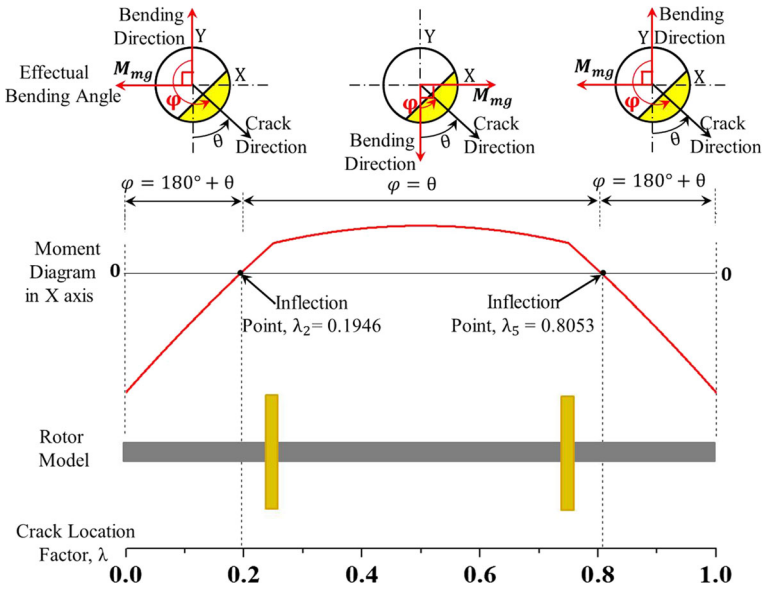

Fig. 7 Effectual bending angle due to gravitational moment only where $M_{mg} = M_{m_s g} + M_{m_d g}$

should be also mentioned that the jump of bending angle from 0° to 360° or 360° to 0° at $\lambda = 0.8053$ is a result of the crack direction changing from leading to following the bending direction.

(c) The other interesting pair of crack locations is at $\lambda = 0.3$ and 0.8335 where the bending angles for all force ratios cross at the same value as those for the balanced shaft. At these two crack locations unbalance force moment is zero (see Fig. 8) and the gravitational force moment is solely responsible for the bending of the shaft. As a result, the cracks will breathe as they would in a balanced shaft.

(d) For $0° < \theta < 180°$, effectual bending angles decrease nonlinearly when crack location increases from the shaft's left end up to the right end (see Fig. 6b–d). This variation of φ with crack location is reversed for the second half of the shaft rotation angle from $180° < \theta < 360°$ (see Fig. 6f–h).

(e) As unbalance force decreases (force ratio increases) the bending angles will progressively approach those for the balanced shaft, which shows that the unbalanced model will be finally in agreement with a balanced model when force ratio is large enough.

Effectual bending angle as a function of shaft rotational angle at some interesting crack locations is shown in Fig. 9 for some chosen force ratios. It is seen that the bending angle for the balanced shaft is one-to-one proportional with the shaft rotation angle. This is a characteristic relationship of the balance shaft previously observed by many researchers. Further, at those locations between two gravitational moment inflection locations λ_2 and λ_5, bending angles are zero at $\theta = 0°$ and they become 180° at locations outside this region, which is consistent with the observation from Fig. 6a. As far as the unbalanced shaft is concerned, it is seen again that at zero gravitational moments λ_2 and λ_5 the deformation of the shaft is solely determined by the unbalance force moment and the bending angle is independent of shaft rotational angle, as shown in Fig. 9b, e. The 180° difference in φ shown in Fig. 9b, e is ascribed to the directional change in the unbalance force moment (see Fig. 8). On the other hand, at zero unbalance force moment locations λ_3 and λ_6 the shaft bending direction is determined by the gravitational moment, so the effectual angle is equal to θ (see Fig. 9c) or $180° + \theta$ (see Fig. 9f), as is the case with a balanced shaft. At other crack locations the bending angle shows a wave-like curve on top of the straight line of the balanced shaft.

The effect of angular position of unbalance force on the bending angle is shown in Fig. 10. It is clear that β has no effect on the bending angle for the balanced shaft because no unbalance force is considered. However, for the unbalanced shaft at zero gravitational moment locations $\lambda_2 = 0.1946$ and $\lambda_5 = 0.8053$, the effectual bending angle is equal to $180° - \beta$ or $360° - \beta$ (see Fig. 10b, e). At zero unbalance force moments $\lambda_3 = 0.3$ and $\lambda_6 = 0.8335$ the bending angle is constant across all β values, which is the same as the balanced shaft (see Fig. 10c, f). As observed earlier, at these four locations ϕ is free of the effect of the force ratio. For all other crack locations there exist two special β values of 135° and 315°. When $\beta = 315°$, unbalance force rotates to gravitational force direction because $\beta + \theta = 315° + 45° = 360°$. Consequently, the shaft deforms at the same direction and has the same φ value as the balanced shaft (see Fig. 10a, d, g). When the unbalance

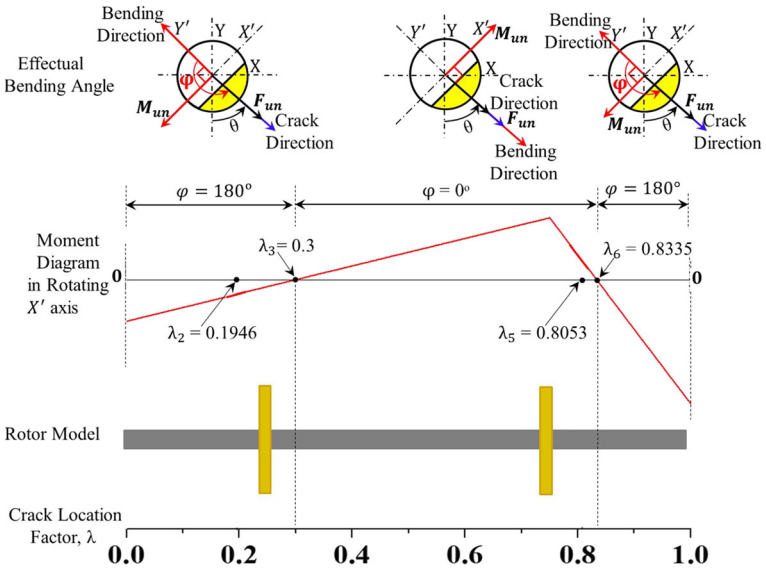

Fig. 8 Bending angle due to unbalance force moment only where $\beta = 0°$

force rotates to the opposite direction to the gravitational force ($\beta + \theta = 135° + 45° = 180°$), the shaft bends in the direction determined by the larger moment between gravitational and the unbalance force moments. In all cases presented here, the gravitational moment is larger than the unbalance force moment. As a result, the bending angle in unbalanced shaft has the same value as that in the balanced shaft.

4.2 Percentage of opening of the crack

Crack breathing behavior can be evaluated quantitatively using a percentage of openings of the crack, Λ, which is displayed in Fig. 11. Similar to the variation of bending angle with the crack location, λ, the percentages of opening for all force ratios are the same at $\lambda_2 = 0.1946$ and $\lambda_5 = 0.8053$, respectively, and approach the value of a balanced shaft at the crack locations $\lambda_3 = 0.3$ and $\lambda_6 = 0.8335$. Shaft stiffness variation with crack location can be divided into three regions at the zero points of gravitational moment λ_2 and λ_5. Increasing λ from 0 to λ_2 leads to a stiffening processing of the shaft because of decreasing Λ, then a softening process from λ_2 to λ_5, and finally a stiffening process again from λ_5 to the right end of the shaft. Zero points of the unbalance force moment λ_3 and λ_6 also divide shaft length into three regions where the overall stiffness of the shaft during a rotation is different from that of the balanced shaft. When the crack is located between λ_3 and λ_6, it is obvious that the percentage of opening of the crack for the unbalanced shaft is larger than that for the balanced counterpart, which indicates that the unbalanced shaft is more flexible than the balanced shaft (also see Fig. 12d). For the remaining two regions, the unbalanced shaft becomes stiffer (also see Fig. 12a, g).

It is also clear in Fig. 11 that variation of Λ with crack location depends strongly on the shaft rotational angle. The percentage of opening Λ for the balanced shaft remains unchanged throughout the entire shaft length when the shaft rotates to 90° and 270°. Λ for the balanced shaft is symmetrical about the shaft middle point. However, for the unbalanced shaft Λ is no longer symmetrical. Moreover, along with the shaft length, a small difference in Λ is seen between the balanced shaft and unbalanced one, when the shaft is at the early stage of rotation or near the completion of rotation as shown in Fig. 11a, b, h.

Percentage of the opening of the crack as a function of shaft rotation angle is depicted in Fig. 12. During a full shaft rotation of 360°, the shaft will generally experience two processes, i.e., a stiffening process corresponding to the decreasing Λ and a softening process corresponding to the increasing Λ. These two processes are seen to be symmetrical about $\theta = 180°$. The flat part of the curve corresponds to either a fully open range ($\Lambda = 100\%$) or a fully closed range ($\Lambda = 0\%$). When a crack is at $\lambda_2 = 0.1946$, the crack in the unbalanced shaft will never open during rotation causing the unbalanced shaft to behave like an uncracked one (see Fig. 12b). A crack in the unbalanced shaft will never close during rotation, and the unbalanced shaft will behave like a shaft with a notch crack at $\lambda_5 = 0.8053$ (see Fig. 12e). At λ_3 and λ_6, a crack will breathe completely like the one in the balanced shaft (see Fig. 12c, f).

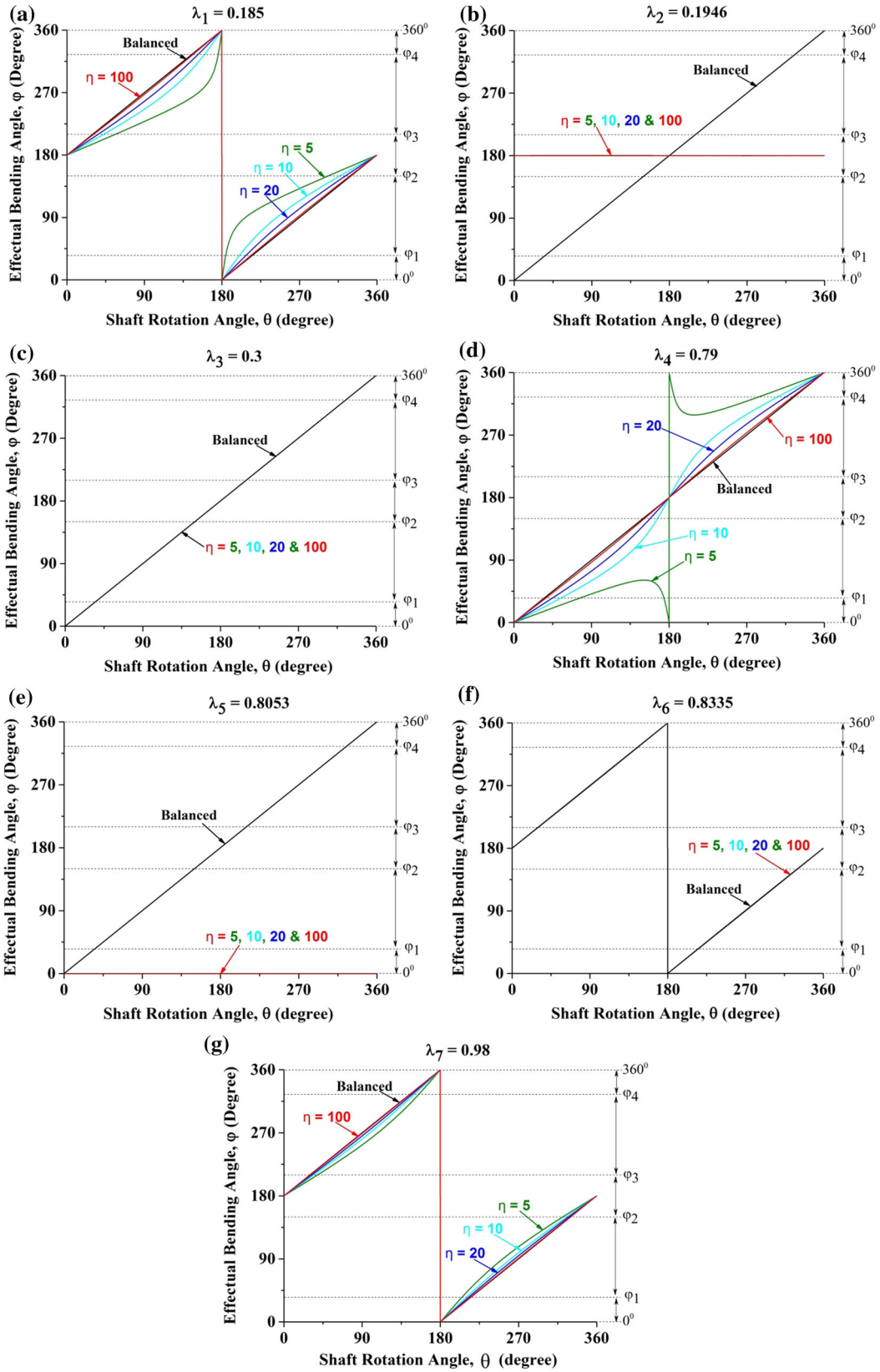

Fig. 9 Effectual bending angle during a full shaft rotation at selected crack locations for different force ratios where $\beta = 0°$

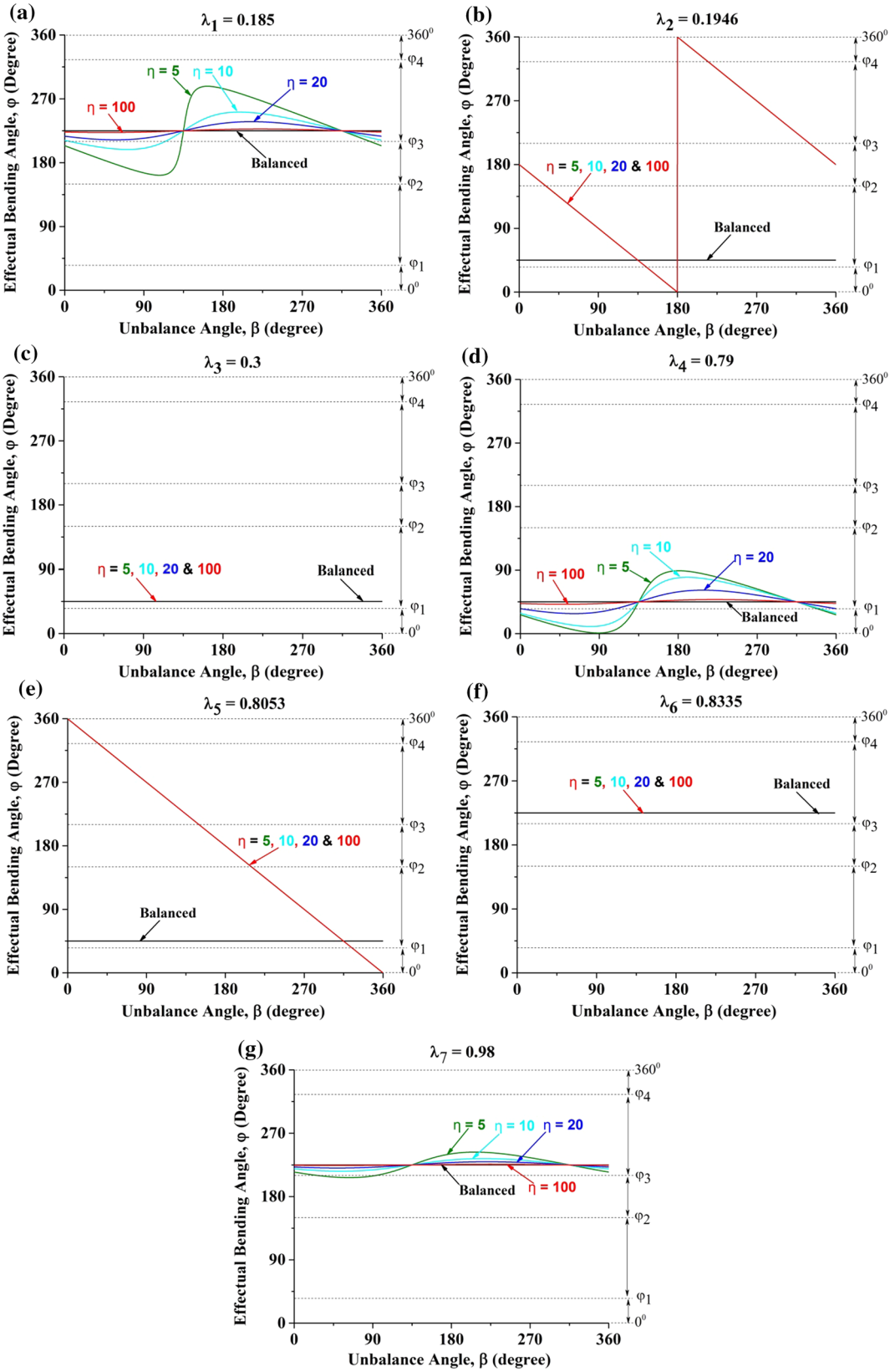

Fig. 10 Effectual bending angle versus unbalance force orientation angle β where $\theta = 45°$

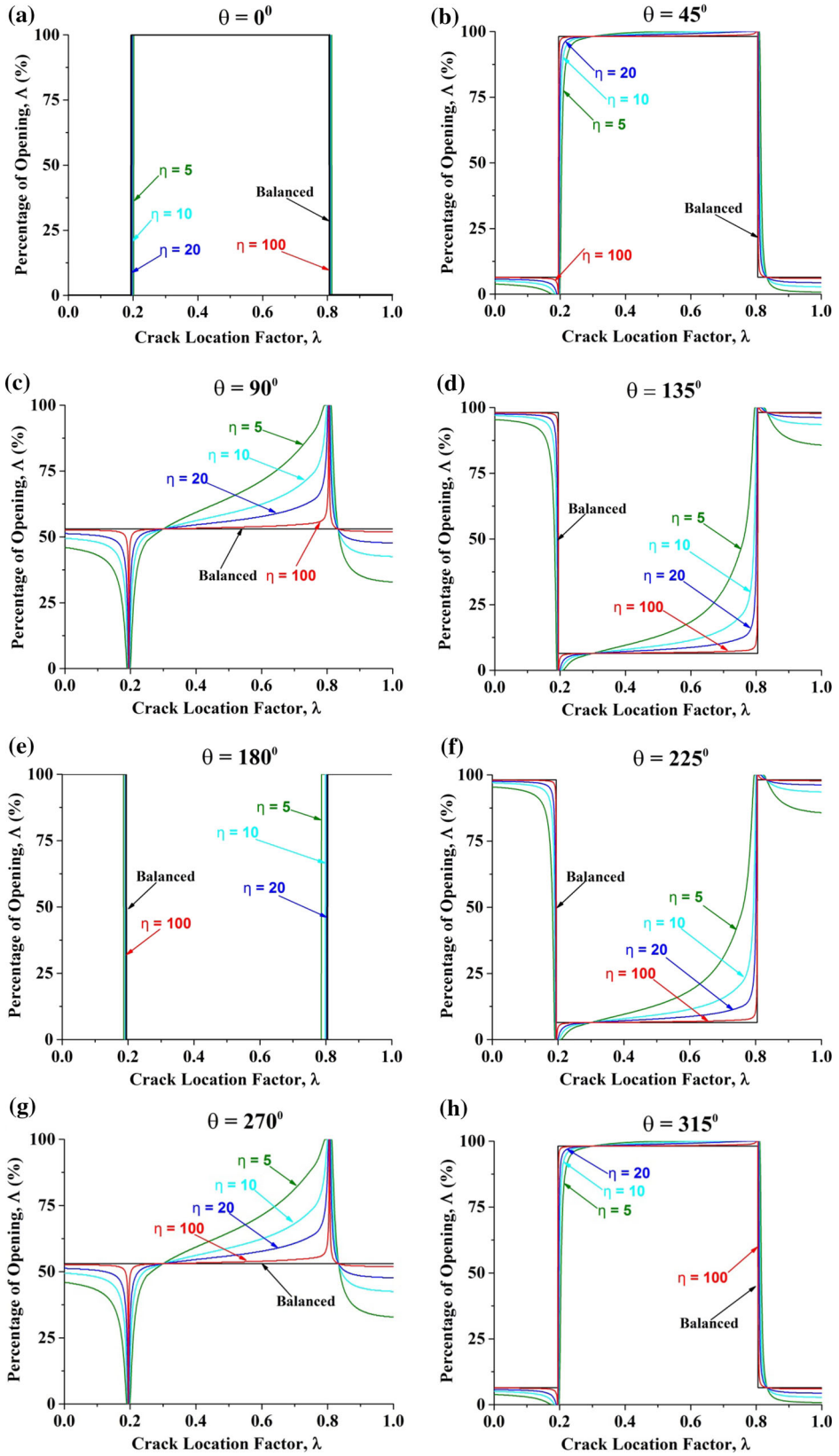

Fig. 11 Percentage of the opening of a crack, Λ, as a function of crack location, λ, for different shaft rotation angles, θ, and force ratios, η, where $\beta = 0°$

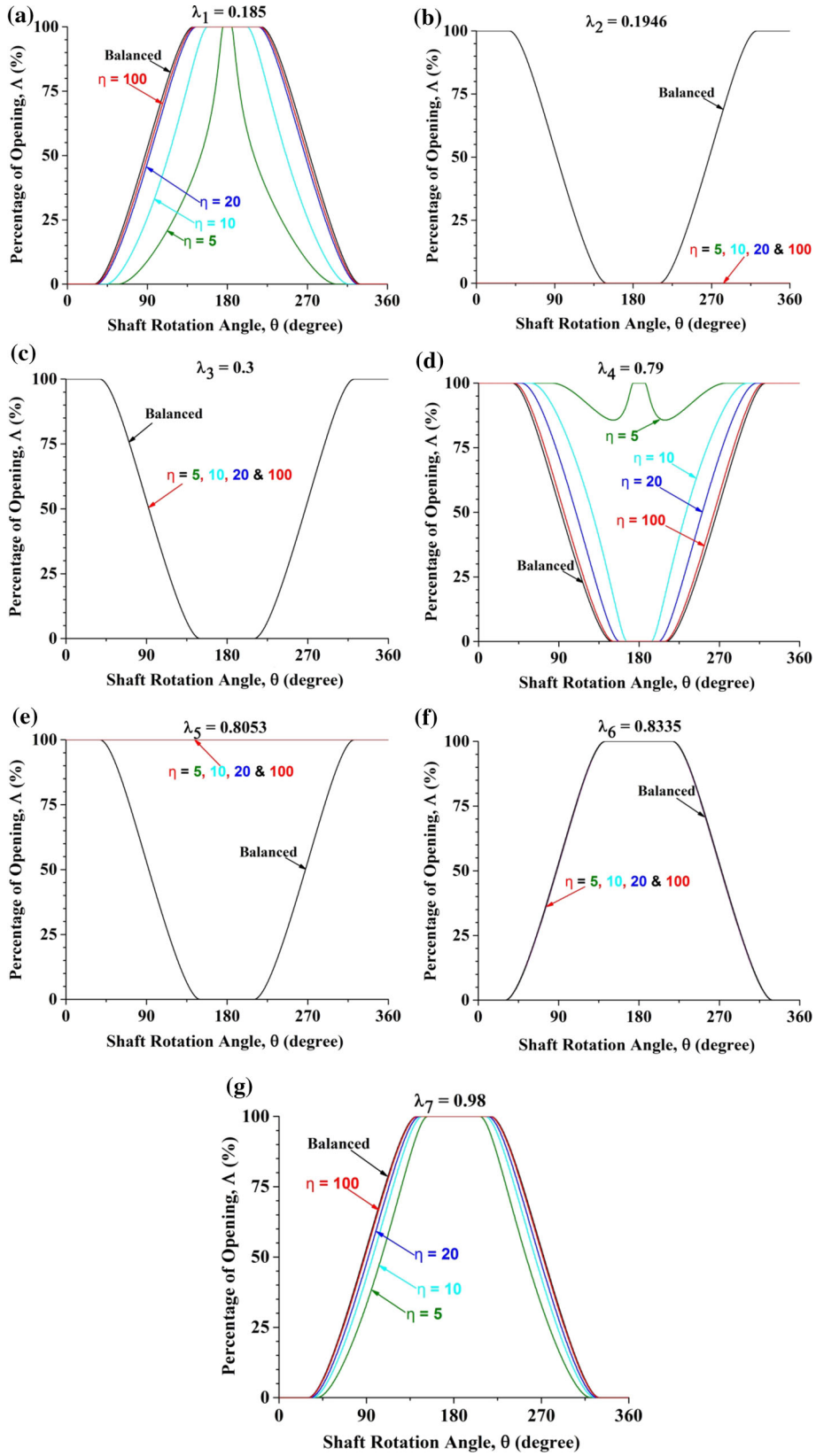

Fig. 12 Percentage of the opening of the crack, Λ, as a function of shaft rotation angle, θ, for different crack locations, λ, and different force ratios, η, where $\beta = 0°$

Figures 11 and 12 represent only a special case where the unbalance force aligns with the crack direction ($\beta = 0°$). For the general unbalance force orientations as shown in Fig. 13, it is identified that the unbalanced shaft is overall stiffer than the balanced one when unbalance force is located in the half area of the cross section opposite to the crack ($90° < \beta < 270°$). In particular, when $\beta = 180°$ the shaft is stiffest (compare Figs. 13d–f). On the other hand, the unbalanced shaft is overall more flexible than the balanced counterpart when the unbalance force is located at the same half area of the cross section of the crack ($0° \leq \beta < 90°$ and $270° < \beta \leq 360°$), and with $\beta = 0°$ the shaft has the smallest stiffness (see Fig. 13a, b, h). The conclusion drawn here from Fig. 13 at $\lambda = 0.79$ also holds true at other crack locations (results not presented). Therefore, the conclusions previously drawn from Fig. 11 regarding the variation of opening percentage with a crack location at $\beta = 0°$ will become opposite when $\beta = 180°$ (or more generally $90° < \beta < 270°$). The original direction of the unbalance force will generate a significant effect on the vibration of the cracked shaft as observed previously. Cheng et al. [46] found that the unbalance orientation played an important role in the peak amplitude of the vibration, where the minimum and maximum vibration amplitude corresponded to the eccentric mass being located at and opposite the crack, respectively.

Two special unbalance force orientations, i.e., $\beta = 90°$ and $\beta = 270°$, are identified as shown in Fig. 13. At these two orientations, the percentage of opening of the crack for the unbalanced shaft is sometimes larger than that of a balanced shaft and sometimes is smaller during a full shaft rotation. The result demonstrates that the overall stiffness of the unbalanced shaft is more or less the same as the balanced shaft (see Fig. 13c, g). It is also seen that the symmetry between the stiffening process and softening process to 180° shaft rotation angle disappears except for $\beta = 0°$ and $\beta = 180°$. The opening percentage as a function of the crack location under selected unbalance force orientation is depicted in Fig. 14. It is clearly seen that the difference in the percentage of the opening along shaft length between two models is larger when $180° < \beta \leq 360°$ ($\beta = 0°$ in Fig. 14a).

4.3 Validation

The numerical validation is performed using a commercial code of Abaqus©/Standard. A complete 3D model of the shaft is employed because there exists no symmetry for the unbalanced shaft. The 3D finite element model of the shaft is presented in Fig. 15.

The crack section is simulated by joining two shafts together using interaction function "tie constraint" that constitutes the intact part of the cracked section. The numerical model is made in such a way that a surface-to-surface contact interaction is defined between the crack faces in order to avoid the interpenetration between them during the closing. To complete the definition of the contact model it is necessary to establish both normal and tangential properties between the crack faces. Regarding the normal properties, "hard" contact is used. This relationship does not allow the penetration of the surfaces in contact at the constraint locations and prevents the transfer of tensile stress across the interface. The chosen tangential property, "rough" friction, introduces an infinite coefficient of friction that avoids all relative sliding motion between the two contacting surfaces. The details of the contact interaction at the crack cross section are shown in Fig. 16. Red zone (upper portion) corresponds to the intact section, and pink zone (lower portion) corresponds to the crack section.

The structured mesh is made by employing a type of elements called C3D8R (8-node linear brick, reduced integration). The mesh has been refined up to a size of elements for which the convergence of results was achieved by means of a mesh sensitivity analysis. In order to get more accurate results, the mesh is much denser near the crack in the transversal and longitudinal direction, as shown in Fig. 17.

In the numerical simulation, the same geometrical and material properties and the load conditions of the cracked shaft are used. The analysis is performed as a succession of static problems with different angular positions of the shaft, θ, with respect to the fixed reference axis. To determine the crack breathing (status of the crack and percentage of opening of the crack) the specific modules in fracture mechanics analysis of Abaqus are used.

Firstly, crack breathing behaviors at two pairs of specific crack locations are evaluated and compared. The statuses of the crack of a balanced and unbalanced shaft for a full shaft rotation angle at $\lambda_3 = 0.3$ and $\lambda_6 = 0.8335$ are depicted in Fig. 18. As it has been already known, analytical model shows that at these two locations the crack will behave like in the balanced shaft with symmetrical and sequential changes during a full shaft rotation, beginning with fully open at $\lambda_4 = 0.3$ and fully closed at $\lambda_6 = 0.8335$. These features are demonstrated completely in Fig. 18. Further, that the crack at $\lambda_2 = 0.1946$ will never open and will never close at $\lambda_5 = 0.8053$ is also well reproduced in the Abaqus simulation, as shown in Fig. 19.

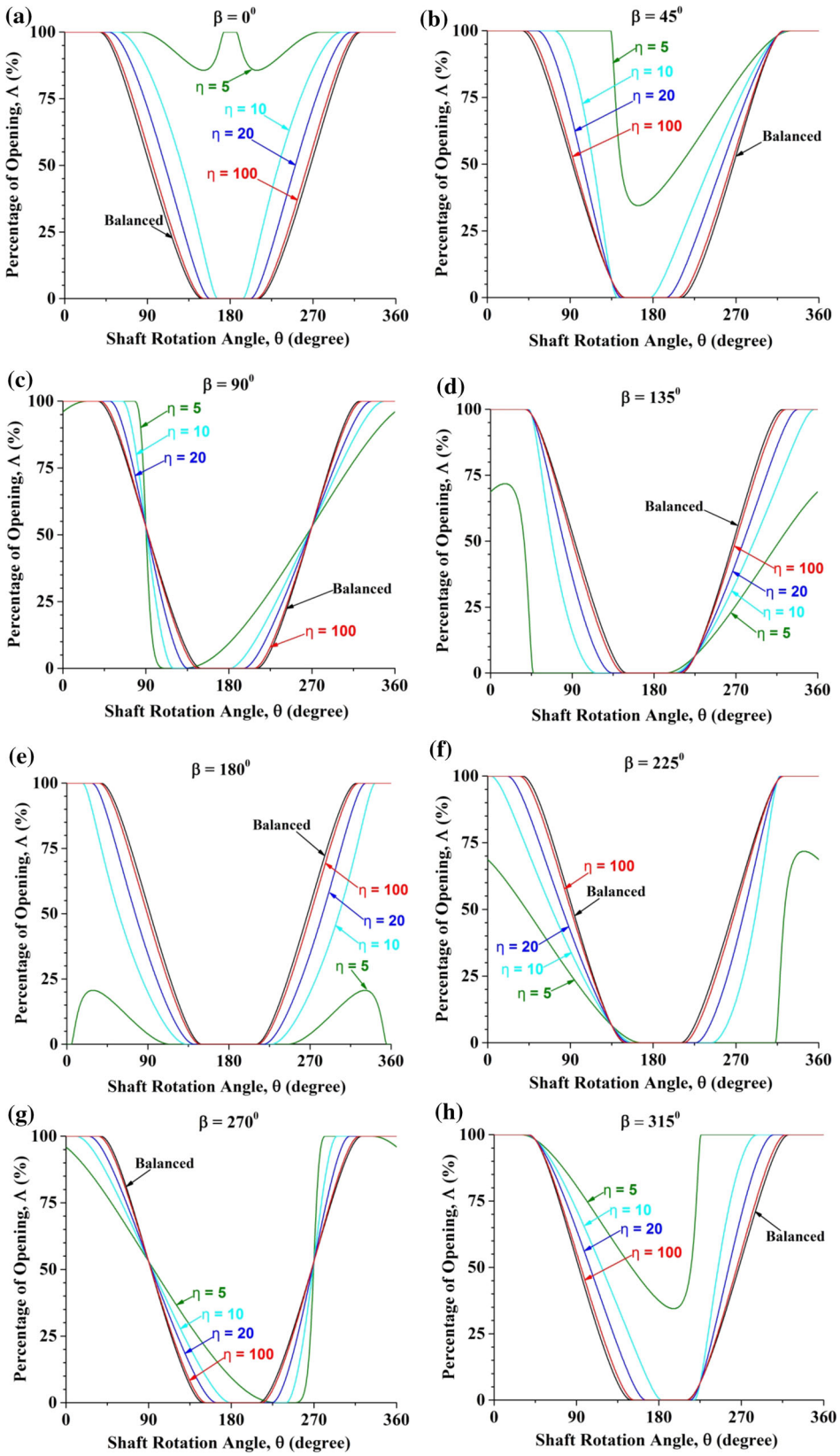

Fig. 13 Effect of unbalance force orientation on the crack breathing behavior at $\lambda = 0.79$

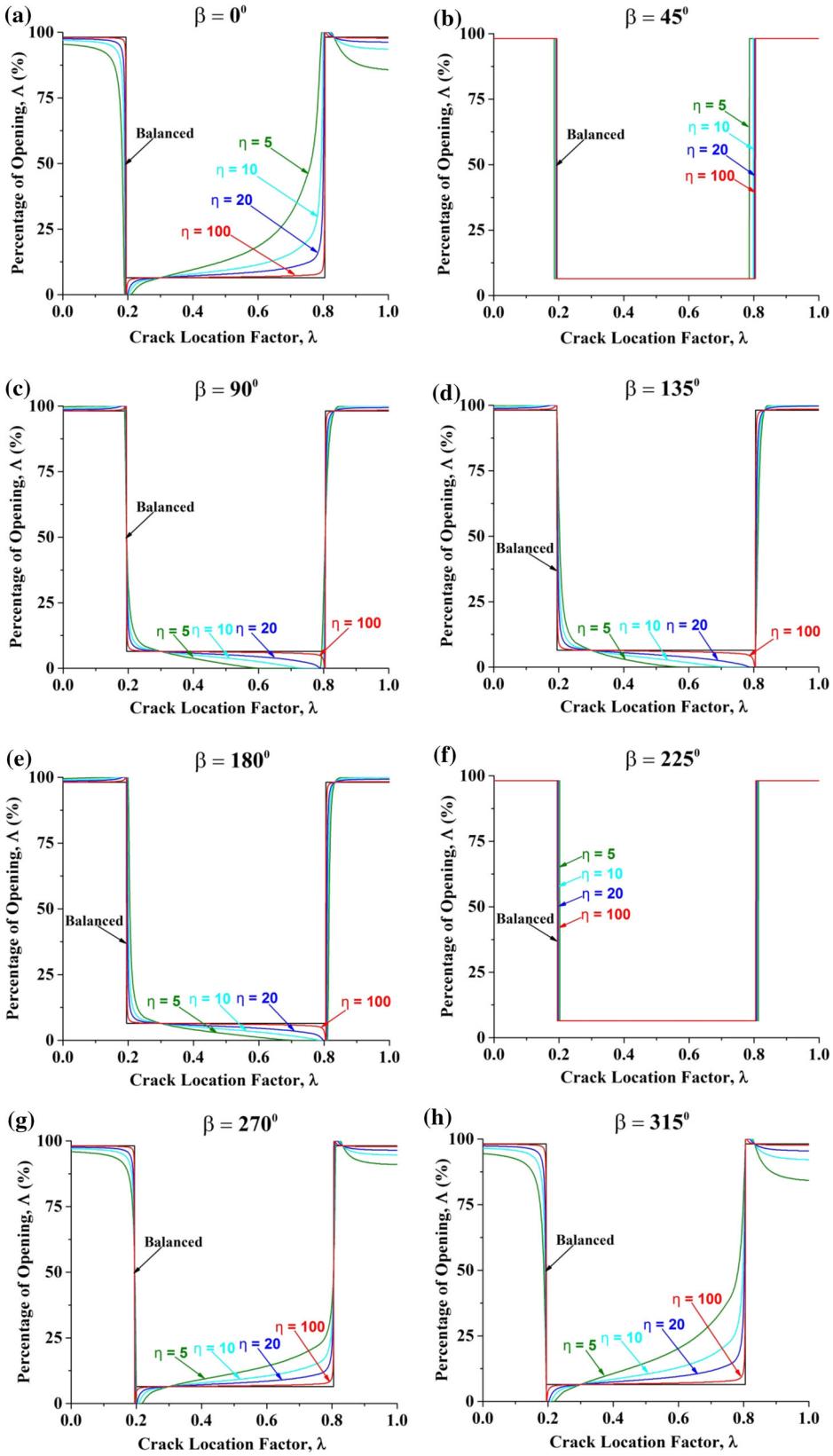

Fig. 14 Effect of unbalance force orientation on the crack breathing behavior where $\theta = 135°$

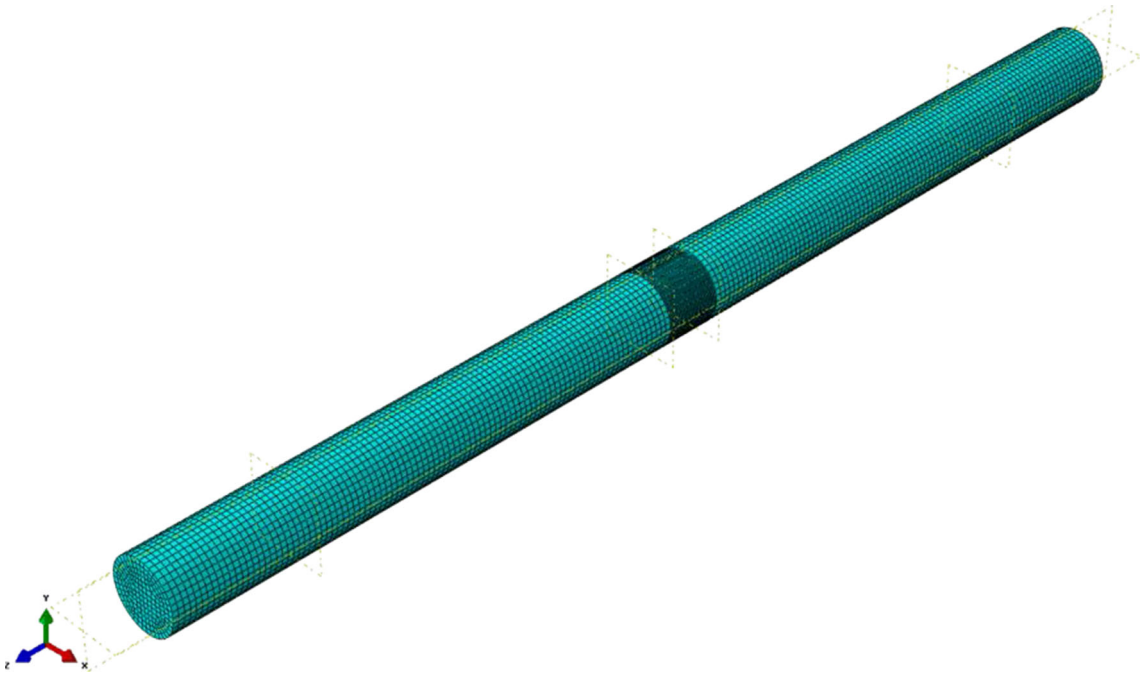

Fig. 15 Complete 3D finite element model of the shaft

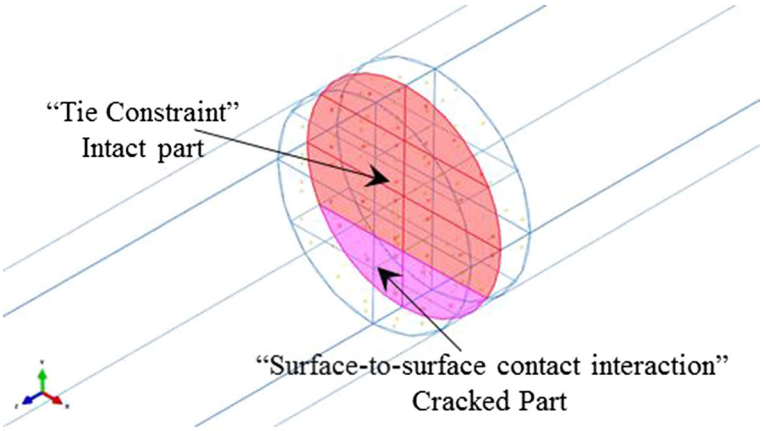

Fig. 16 Surface-to-surface contact interaction

Secondly, a quantitative comparison through a percentage of the opening is displayed in Fig. 20 for the balanced shaft and unbalanced one ($\eta = 10$ & $\beta = 0°$ and $\lambda_4 = 0.5$). In general, it is found that the proposed analytical model captures the main features of the crack breathing and is in good agreement with Abaqus simulation. The possible errors may be attributed to curved boundary between opening area and the closed area of the crack in Abaqus simulation (see Fig. 18) and the straight boundary line in the balanced and unbalanced models (see Fig. 5). Curved boundary line was also observed in the previous Abaqus simulation for the balanced shaft [3] and unbalanced shaft with simple support ends [5,49]. Moreover, it can be inferred that the calculations for the unbalanced model using Eqs. (6) and (7) do not introduce any further large error since the error between the present unbalanced model and Abaqus simulation in Fig. 20b is more or less the same as that between the balanced shaft and Abaqus simulation in Fig. 20a.

4.4 The area moment of inertia at the crack cross section

Crack breathing behavior leads to a change in the shaft stiffness [40]. Studying the change in the area moment of inertia of a cracked shaft can link the breathing mechanism to the stiffness matrix in the rotor and ultimately

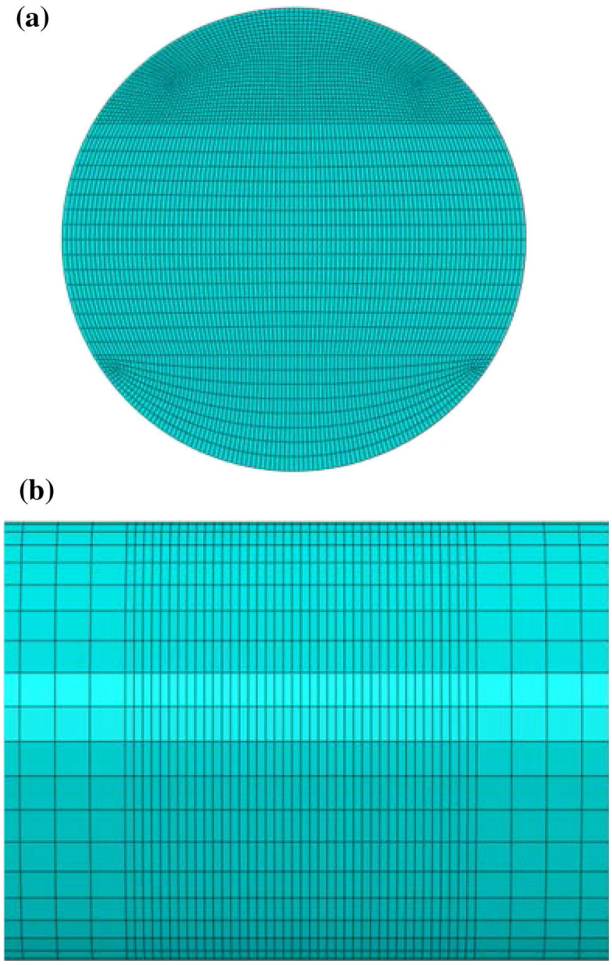

Fig. 17 Mesh near the crack cross section in **a** transversal and **b** longitudinal direction

calculate the vibration responses. Al-Shudeifat et al. [39] developed an iterative method to calculate the area moment of inertia of the time-varying non-cracked area $A_{ce}(t)$ for a balanced shaft (shown in Fig. 5a). In their work the effect of the unbalance force and shaft support condition on the crack breathing is neglected. The time-varying non-cracked area $A_{ce}(t)$ is equal to $A_1 + A_2(t)$, where A_1 is the area of the uncracked element (see Fig. 2a) and $A_2(t)$ is the area of the closed portion of the crack at time t (see Fig. 5). Firstly, the method calculates the areas $A_2(t)$ and A_1 and their respective centroid locations to obtain the overall magnitude and centroid location of $A_{ce}(t)$. Then the area moments of inertia of $A_{ce}(t)$ about the centroidal axes $\bar{X}$ and $\bar{Y}$ are obtained.

For the unbalanced system as shown in Fig. 5b, the modified centroid coordinates X_{ce} and Y_{ce} of non-cracked area $A_{ce}(t)$ about the original non-rotated coordinate X- and Y-axes are described in Eqs. (14) and (15), where X'_{ce} and Y'_{ce} are the centroid coordinates with respect to the X'- and Y'-axes, which are the same as those with respect to the X- and Y-axes in the balanced model.

$$X_{ce} = X'_{ce}\cos\delta - Y'_{ce}\sin\delta \tag{14}$$

$$Y_{ce} = X'_{ce}\sin\delta + Y'_{ce}\cos\delta. \tag{15}$$

The area moment of inertia of the non-cracked area about the unbalanced rotor's $\bar{X}$ and $\bar{Y}$ is obtained by comparing the geometric similarity between two models. When the bending angle in the unbalanced shaft is equal to the shaft rotational angle in the balanced shaft, the area moments of inertia of the non-cracked area about respective $\bar{X}$ and $\bar{Y}$ in two models are also equal. After obtaining the area moments of inertia for the balanced shaft using expressions in [39], the area moments of inertia with different force ratios at a

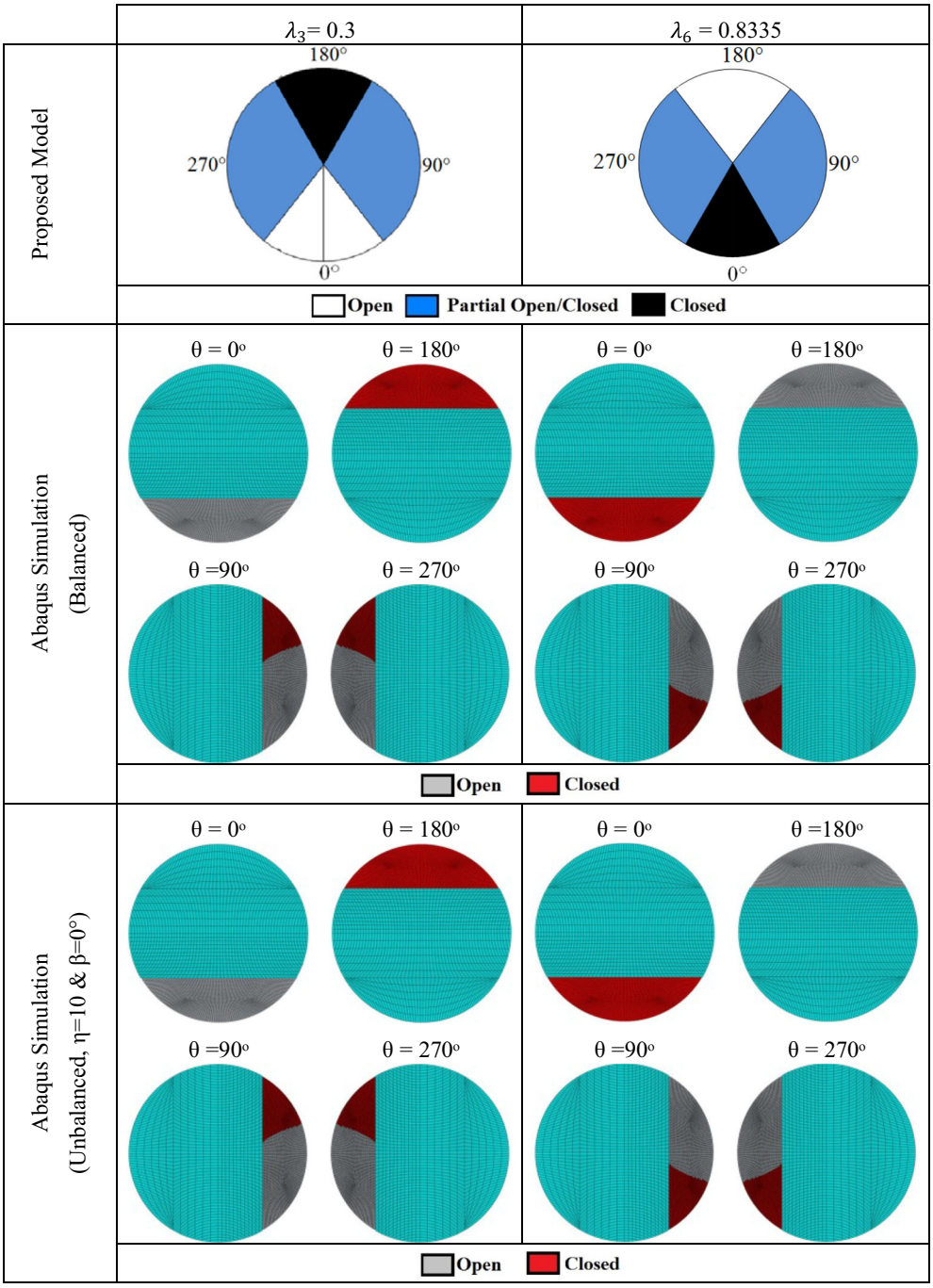

Fig. 18 Statuses of crack of a full shaft rotation angle at crack locations, $\lambda_3 = 0.3$ and $\lambda_6 = 0.8335$

shaft rotational angle for an unbalanced shaft are obtained using the relation between bending angle and shaft rational angle in Eq. 7.

4.4.1 Orbit of the centroid of uncracked area

The centroid orbits of uncracked area, $A_{ce}(t)$, about the X- and Y-axes at different crack locations under different force ratios are illustrated in Fig. 21. Although effectual bending angle, status of the cracks and percentage of opening for the balanced shaft all depend on the crack location, the orbits remain unchanged

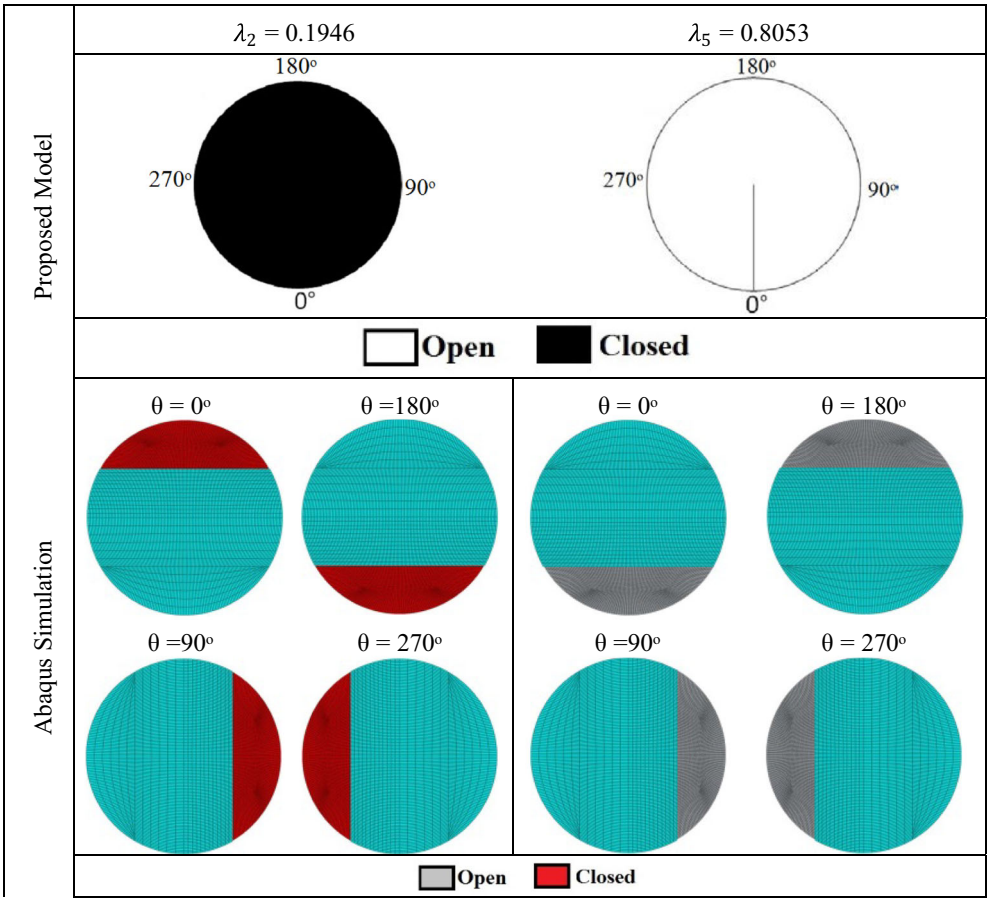

Fig. 19 Statuses of crack of an unbalanced shaft ($\eta = 10$ & $\beta = 0°$) for a full shaft rotation angle at crack locations $\lambda_2 = 0.1946$ and $\lambda_5 = 0.8053$

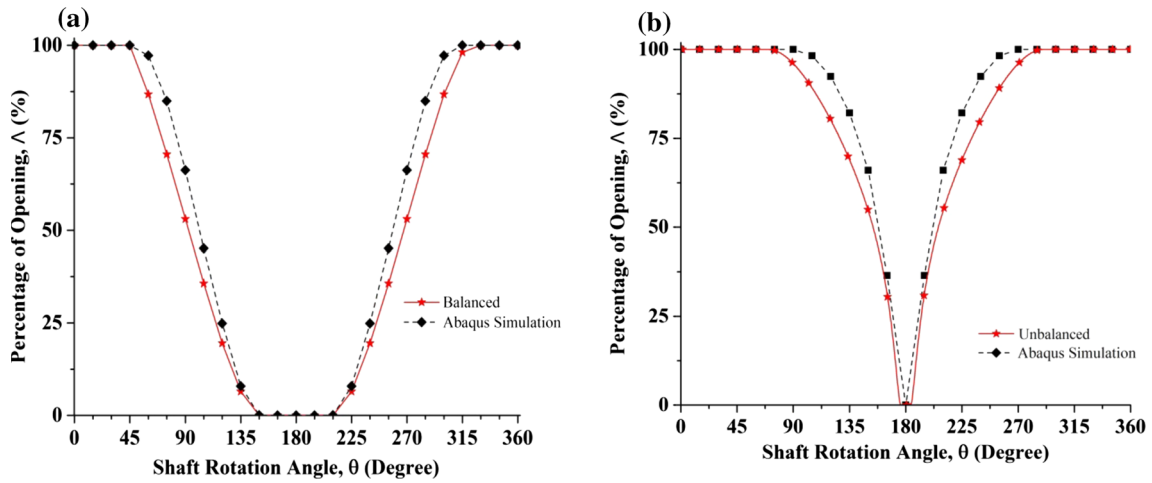

Fig. 20 Percentage of opening of the crack as a function of shaft rotation angle at crack location $\lambda_4 = 0.5$ for **a** balanced and **b** unbalanced ($\eta = 10 \& \beta = 0°$) shaft

along the crack length. Similar to the previous results, centroid orbit for the unbalanced shaft also has special behaviors at four crack locations. It should be noted that at λ_2 the orbit is just a single point lying on the origin indicating a fully closed never-opened crack and is independent of the force ratio (see Fig. 21b). At λ_5, a circle is seen indicating a fully opened crack also independent of force ratio (see Fig. 21e). Further, the orbit for the

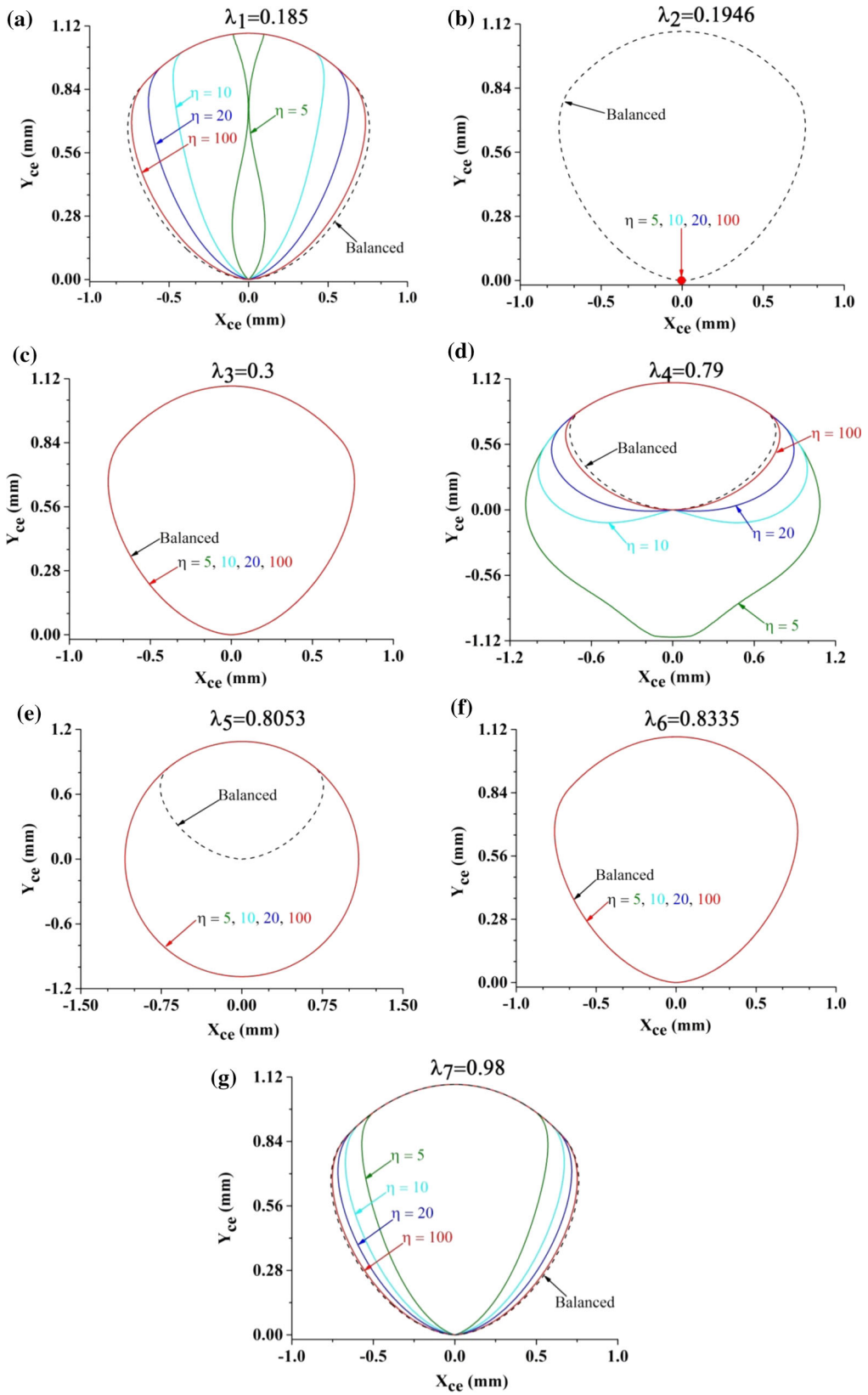

Fig. 21 Orbits of the centroid of uncracked area, $A_{ce}(t)$, for different crack locations, λ, and weight–unbalance force ratios, η, where $\beta = 0°$

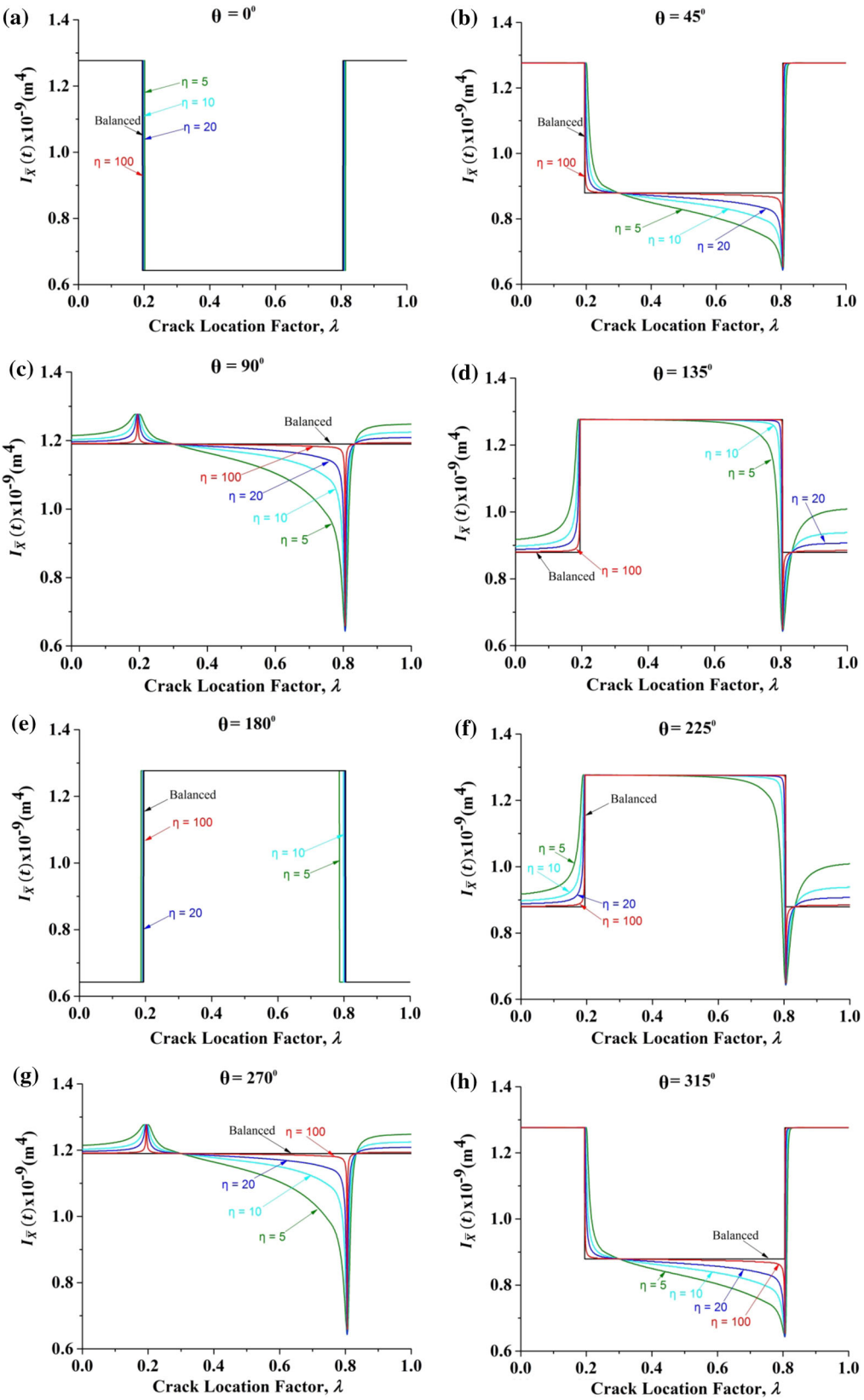

Fig. 22 Area moment of inertia $I_{\bar{X}}$ of uncracked area, $A_{ce}(t)$, along the shaft length where $\beta = 0°$

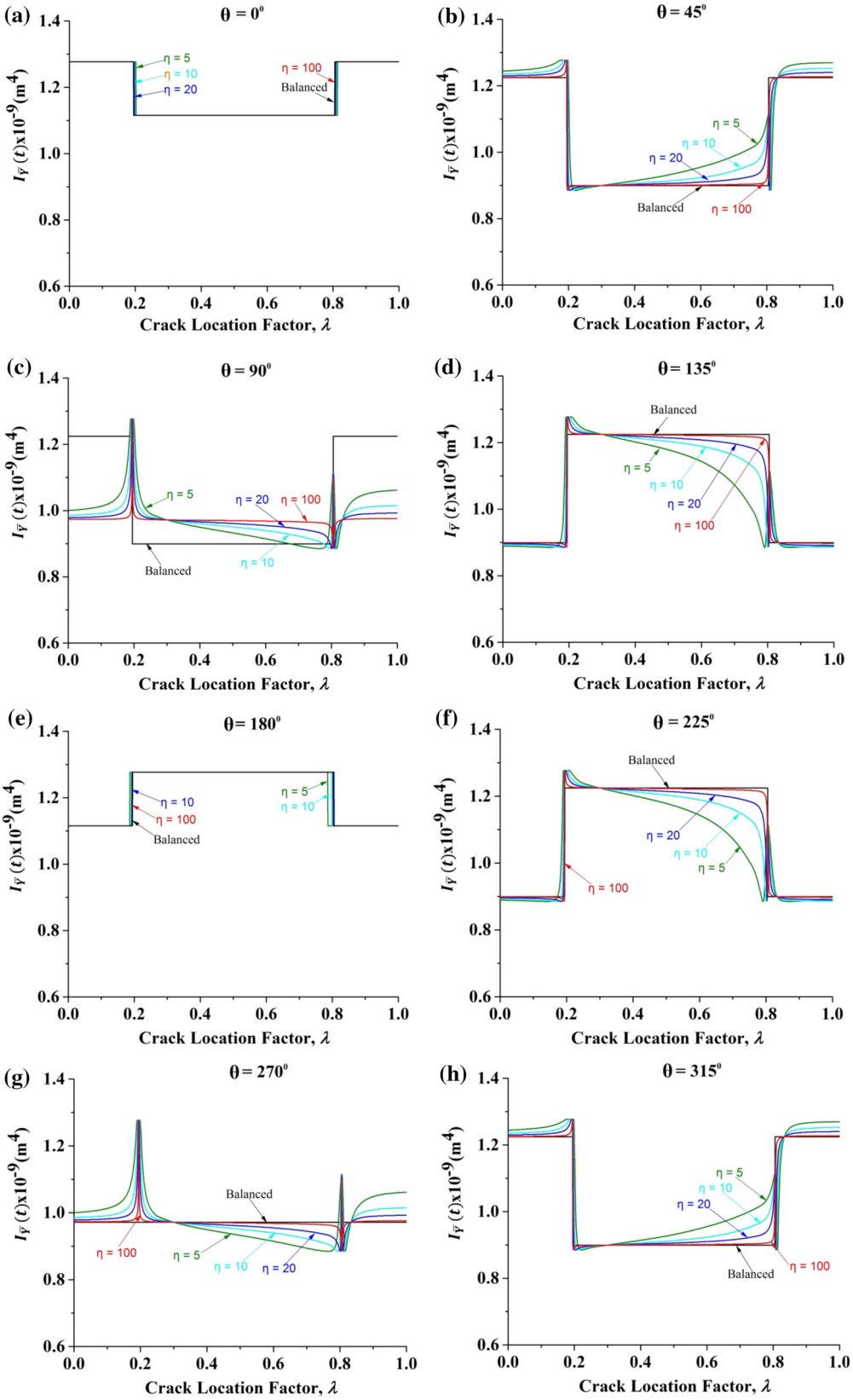

Fig. 23 Area moment of inertia $I_{\bar{Y}}$ of uncracked area, $A_{ce}(t)$, along the shaft length where $\beta = 0°$

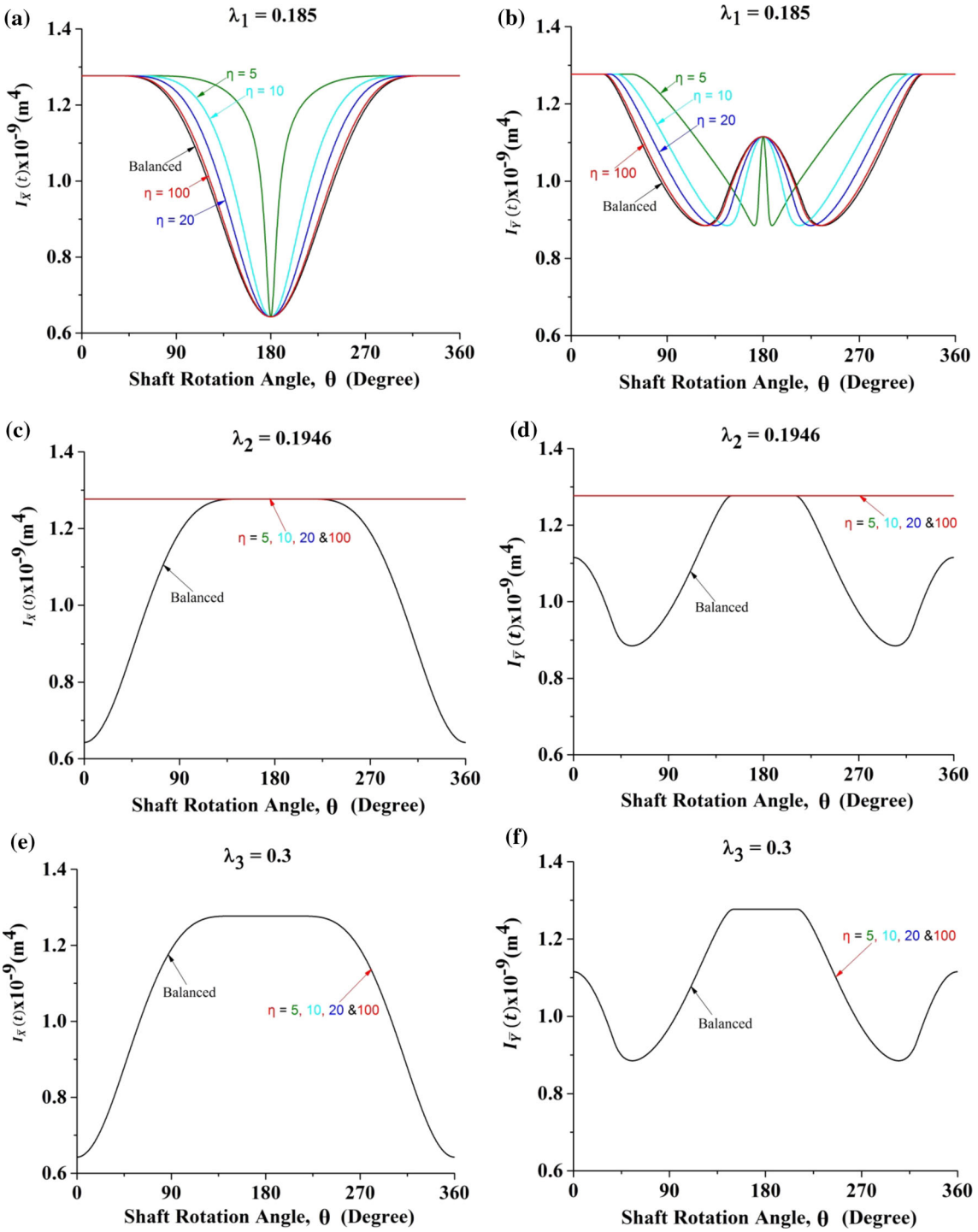

Fig. 24 Area moment of inertia of $I_{\bar{X}}$ and $I_{\bar{Y}}$ of uncracked area, $A_{\text{ce}}(t)$, over a full shaft rotation, θ, where $\beta = 0°$

unbalanced shaft at λ_3 and λ_6 overlaps that of the balanced shaft (see Fig. 21c, f). The orbit at other locations generally changes the shape and largeness of the circle depending on the crack location and force ratio. In general, an enlarged orbit means a small overall stiffness of the shaft. When the orbit for the balanced shaft encircles that for the unbalanced shaft as shown in Fig. 21a, g, the overall stiffness of the balanced shaft is smaller than that of the unbalanced shaft and vice versa as shown in Fig. 21d. The observations on the orbit are in agreement with previous results.

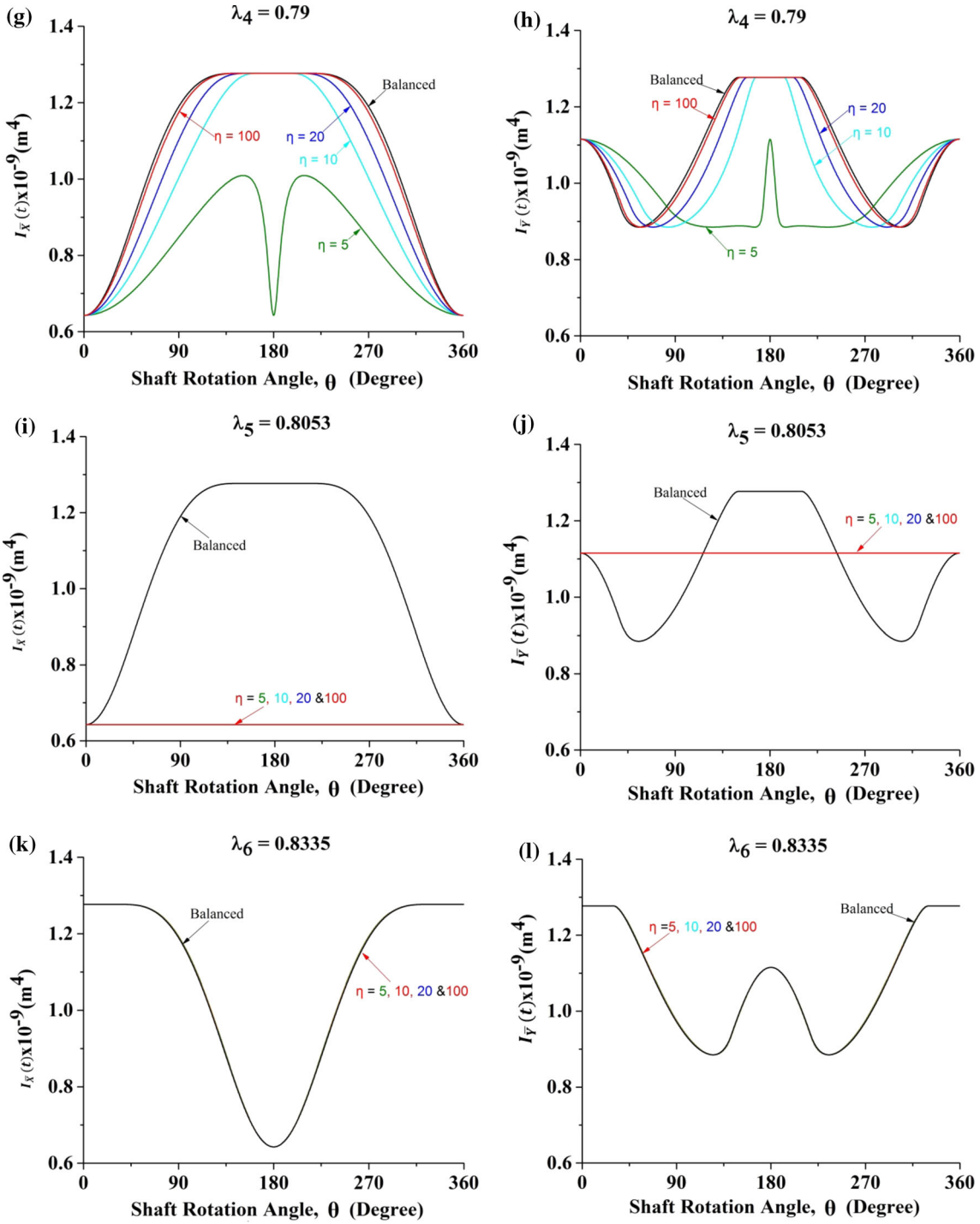

Fig. 24 continued

4.4.2 Area moment of inertia of uncracked area

The ultimate purpose of this study is to establish an easy-to-use model to calculate the area moments of inertia at the cracked cross section for the unbalanced shaft. These area moments of inertia constitute the elements of the local stiffness matrix of a cracked shaft element [26,36,51]. Then, the cracked shaft vibration response can be calculated numerically by solving the equations of motion of the system.

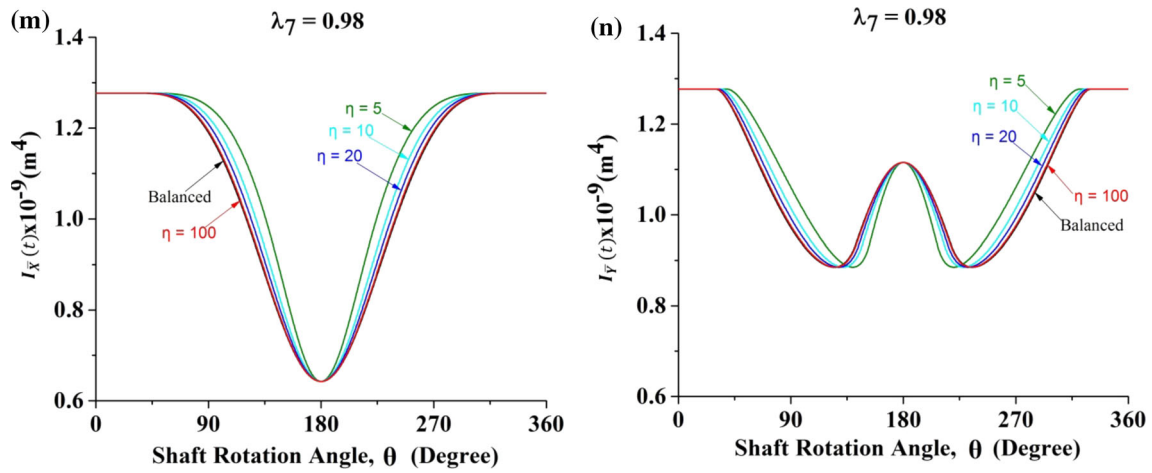

Fig. 24 continued

The area moments of inertia along the shaft length in relation to centroid axes $\bar{X}$ and $\bar{Y}$ are illustrated in Figs. 22, 23, 24, 25 and 26. The value for $I_{\bar{X}}$ that corresponds to a fully closed crack status is 1.27×10^{-9} m^4 (same as uncracked shaft $\frac{\pi R^4}{4}$) and 0.65×10^{-9} m^4 for a fully opened crack (compare Figs. 14a and 24a). $I_{\bar{X}}$ changes between these two values during shaft rotation and along the shaft length. The value for $I_{\bar{Y}}$ at these two crack statuses is 1.27×10^{-9} m^4 and 1.11×10^{-9} m^4, respectively (see Fig. 25a). It is interesting to note that $I_{\bar{Y}}$ could be larger for a fully open crack than for a partially open/closed crack. Further, variation of $I_{\bar{Y}}$ with shaft rotational angle, θ, differs from that of $I_{\bar{X}}$, showing a dual minimum behavior, as shown in Fig. 26. As far as the effect of the crack location is concerned, previous conclusions on the crack breathing behavior at two pairs of special locations can also be deduced from the area moment of inertia (see Fig. 24c–f, i–l). It is expected that large difference between two models in the area moment of inertia during shaft rotation and along shaft length will generate large difference in vibrations accordingly. Further study on the vibration behavior of a cracked rotor under the influence of unbalance force is currently under the way.

The current work presents a quasi-static analysis of crack breathing functions under the effect of unbalance force and extends our understanding in the field. However, the actual crack breathing is very complicated and can be affected by many factors, in particular vibration-induced effects like shaft whirling, excited by unbalance force, and gyroscopic moment. Under some vibration conditions, these effects on the shaft bending angle may no longer be ignored. As such, further study on the vibration-induced crack breathing should be an interesting area.

5 Conclusions

In this paper, a new unbalanced model is developed to study crack breathing behavior in terms of crack location along shaft length, shaft rotational angle, unbalance force orientation, and the ratio of gravitational force to unbalance force. The results are also compared with those of the balanced shaft and validated by Abaqus simulation.

For the balanced shaft at $\theta = 90°$ and 270°, the opening percentage of the crack (or crack status) remains unchanged along the whole shaft length. At the other shaft rotational angles, the opening percentage of the crack can be divided into three regions at the locations of zero gravitational moments $\lambda_2 = 0.1946$ and $\lambda_5 = 0.8053$. In each region, the opening percentage of the crack is a constant. However, the crack status in the middle region is different from two side regions. This behavior is caused by an 180° change in the bending angle at λ_2 and λ_5. Moreover, the opening percentage of the crack is symmetrical about the shaft middle point.

Overall, notably different crack breathing behaviors have been identified for the unbalanced shaft. An unbalanced shaft is just like an uncracked shaft when the crack is at $\lambda_2 = 0.1946$, and a crack at $\lambda_5 = 0.8053$ is just like a notch and will never close. At λ_3 and λ_6, a crack in the unbalanced shaft will behave completely like the one in the balanced shaft. These unique crack breathing mechanisms will never happen in a balanced shaft.

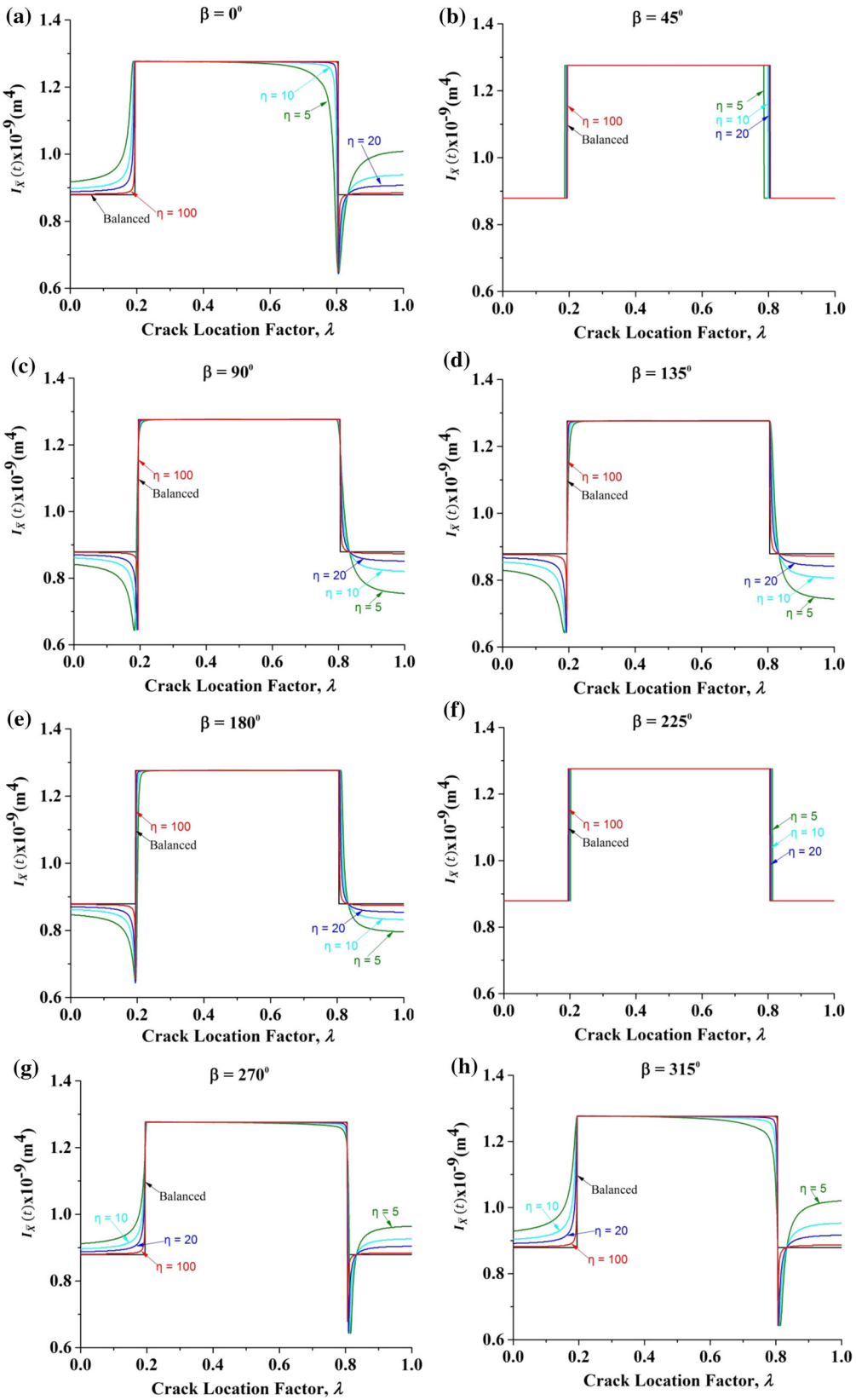

Fig. 25 Area moment of inertia of $I_{\bar{X}}$ of uncracked area, $A_{\text{ce}}(t)$, for different β along the shaft length where $\theta = 135°$

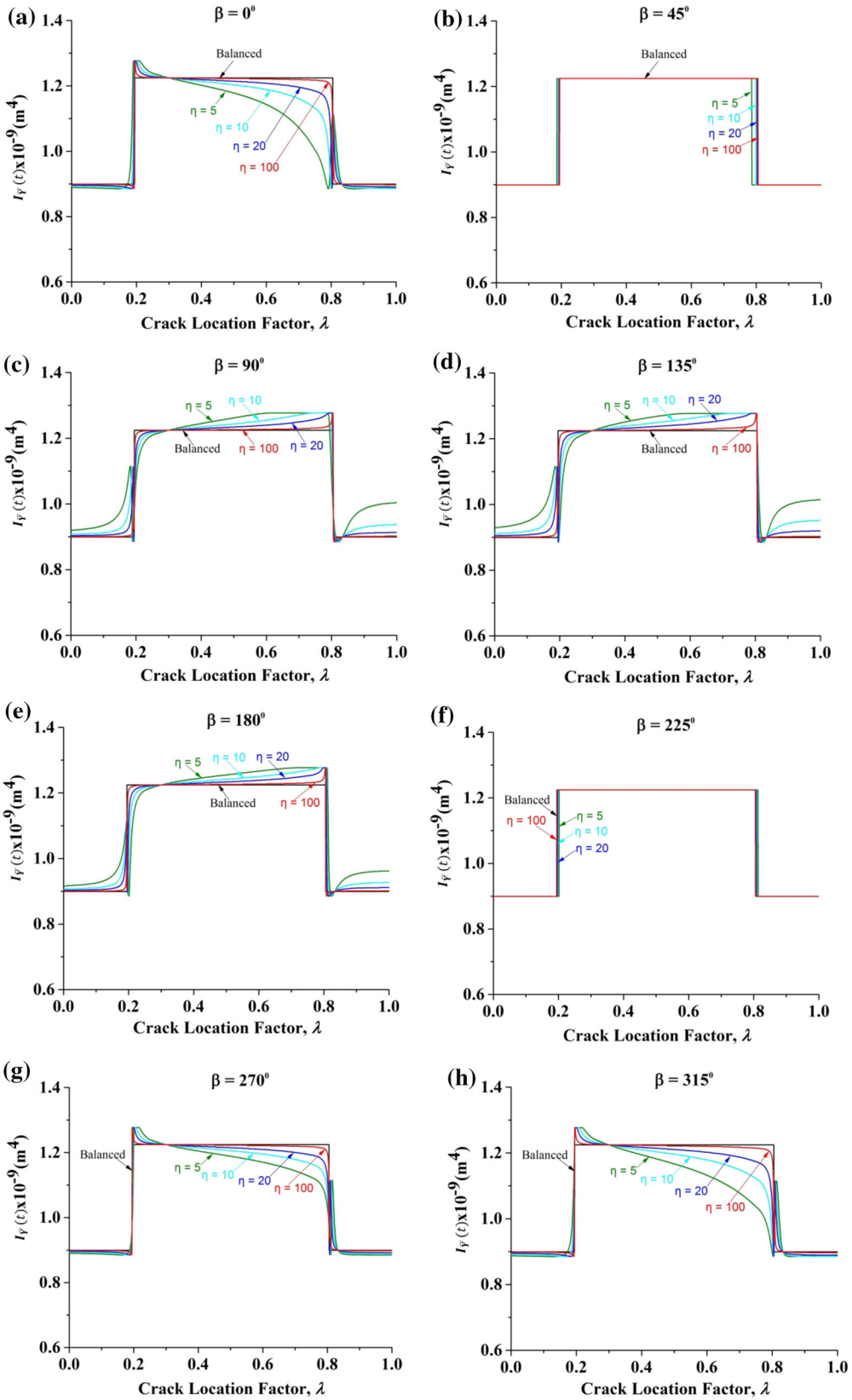

Fig. 26 Area moment of inertia of $I_{\bar{Y}}$ of uncracked area, $A_{\text{ce}}(t)$, for different β along the shaft length where $\theta = 135°$

Shaft stiffness variation with crack location can be divided into three regions at the locations of zero gravitational moments λ_2 and λ_5. When an unbalanced force is located in the same half area of the cross section of the crack ($0° \leq \beta < 90°$ and $270° < \beta \leq 360°$), an increase in λ from 0 to λ_2 will lead to the stiffening of the shaft because of a decrease in Λ. Also, a softening process from λ_2 to λ_5 and the other stiffening process again from λ_5 to the right end of the shaft will occur. Zero unbalance force moment locations, λ_3 and λ_6, also divide shaft length into three regions. When the crack is in the middle region, the unbalanced shaft is more flexible than the balanced shaft. In the remaining two regions the unbalanced shaft is stiffer. These trends will become opposite when unbalance force is located in the half area of the cross section opposite to the crack ($90° < \beta < 270°$). Further, when unbalance force has a right angle relative to the crack direction ($\beta = 90°$ and $\beta = 270°$), the overall stiffness of the unbalanced shaft is more or less the same as the balanced shaft. Second area moments of inertia are also calculated to establish a link between the present work and the prediction of the vibration response of cracked rotor. Finally, the unbalanced shaft model developed in this work will gradually approach the balanced shaft model when the unbalance force decreases.

The present model has identified the unique crack breathing behaviors under the influence of unbalance force and rotor physical and dimensional properties, showing the strong dependence of the breathing mechanism on the crack location. The developed model can be further used to obtain local stiffness matrix of a cracked shaft element and then to study the vibration response of a cracked rotor, in particular near the shaft critical speeds or where rotor-weight-dominant assumption on the crack breathing no longer holds.

Acknowledgements The authors would like to gratefully acknowledge the financial support given by the School of Computing, Engineering, and Mathematics, Western Sydney University, Australia, for the development of this research.

References

1. Kumar, C., Rastogi, V.: A brief review on dynamics of a cracked rotor. Int. J. Rotat. Mach. **2009**, 758108, 6 p (2009). doi:10.1155/2009/758108
2. Georgantzinos, S.K., Anifantis, N.K.: An insight into the breathing mechanism of a crack in a rotating shaft. J. Sound Vib. **318**, 279–295 (2008)
3. Bachschmid, N., Pennacchi, P., Tanzi, E.: Cracked Rotors: A Survey on Static and Dynamic Behaviour Including Modelling and Diagnosis. Springer, Berlin (2010)
4. Liong, R.T., Proppe, C.: Implementation of a cohesive zone model for the investigation of the dynamic behavior of a rotating shaft with a transverse crack. Proc. Appl. Math. Mech. **10**, 125–126 (2010)
5. Rubio, L., Fernández-Sáez, J.: A new efficient procedure to solve the nonlinear dynamics of a cracked rotor. Nonlinear Dyn. **70**, 1731–1745 (2012)
6. Pennacchi, P., Bachschmid, N., Vania, A.: A model-based identification method of transverse cracks in rotating shafts suitable for industrial machines. Mech. Syst. Signal Process. **20**, 2112–2147 (2006)
7. Guo, C., Al-Shudeifat, M.A., Yan, J., Bergman, L.A., McFarland, D.M., Butcher, E.A.: Application of empirical mode decomposition to a Jeffcott rotor with a breathing crack. J. Sound Vib. **332**, 3881–3892 (2013)
8. Kulesza, Z.: Dynamic behavior of cracked rotor subjected to multisine excitation. J. Sound Vib. **333**, 1369–1378 (2014)
9. Yan, G., De Stefano, A., Matta, E., Feng, R.: A novel approach to detecting breathing-fatigue cracks based on dynamic characteristics. J. Sound Vib. **332**, 407–422 (2013)
10. Guo, J., Huang, X., Cui, Y.: Design and analysis of robust fault detection filter using LMI tools. Comput. Math. Appl. **57**, 1743–1747 (2009)
11. Xiang, J., Zhong, Y., Chen, X., He, Z.: Crack detection in a shaft by combination of wavelet-based elements and genetic algorithm. Int. J. Solids Struct. **45**, 4782–4795 (2008)
12. Andreaus, U., Casini, P., Vestroni, F.: Frequency reduction in elastic beams due to a stable crack: numerical results compared with measured test data. Eng. Trans. **51**, 87–101 (2003)
13. Andreaus, U., Casini, P., Vestroni, F.: Nonlinear features in the dynamic response of a cracked beam under harmonic forcing. In: Proceedings of DETC'05, 2005 ASME International Design Engineering Technical Conferences and Computers and Information in Engineering Conference, Long Beach, California, USA, September 24–28, vol. 6, pp. 2083–2089 (2005)
14. Andreaus, U., Casini, P., Vestroni, F.: Nonlinear dynamics of a cracked cantilever beam under harmonic excitation. Int. J. Nonlinear Mech. **42**, 566–575 (2007)
15. Andreaus, U., Baragatti, P.: Fatigue crack growth, free vibrations and breathing crack detection of aluminium alloy and steel beams. J. Strain Anal. Eng. Des. **44**, 595–608 (2009)
16. Andreaus, U., Baragatti, P.: Cracked beam identification by numerically analysing the nonlinear behaviour of the harmonically forced response. J. Sound Vib. **330**, 721–742 (2011)
17. Andreaus, U., Baragatti, P.: Experimental damage detection of cracked beams by using nonlinear characteristics of forced response. Mech. Syst. Signal Process. **31**, 382–404 (2012)
18. Andreaus, U., Casini, P.: Identification of multiple open and fatigue cracks in beam-like structures using wavelets on deflection signals. Contin. Mech. Thermodyn. **28**, 361–378 (2016)
19. Andreaus, U., Baragatti, P., Casini, P., Iacoviello, D.: Experimental damage evaluation of open and fatigue cracks of multi-cracked beams by using wavelet transform of static response via image analysis. Struct. Control Health Monit. **24**, 1–16 (2017)

20. Dimarogonas, A., Papadopoulos, C.: Vibration of cracked shafts in bending. J. Sound Vib. **91**, 583–593 (1983)
21. Papadopoulos, C., Dimarogonas, A.: Coupled longitudinal and bending vibrations of a rotating shaft with an open crack. J. Sound Vib. **117**, 81–93 (1987)
22. Papadopoulos, C.A., Dimarogonas, A.D.: Stability of cracked rotors in the coupled vibration mode. ASME. J. Vib. Acoust. Stress Reliab. **110**(3), 356–359 (1988). doi:10.1115/1.3269525
23. Chan, R., Lai, T.: Digital simulation of a rotating shaft with a transverse crack. Appl. Math. Model. **19**, 411–420 (1995)
24. Yang, B., Suh, C.S., Chan, A.K.: Characterization and detection of crack-induced rotary instability. J. Vib. Acoust. Trans. ASME **124**, 40–48 (2002)
25. Sekhar, A.S.: Crack detection through wavelet transform for a run-up rotor. J. Sound Vib. **259**, 461–472 (2003)
26. Sinou, J.-J.: Effects of a crack on the stability of a non-linear rotor system. Int. J. Nonlinear Mech. **42**, 959–972 (2007)
27. Sinou, J.-J.: Detection of cracks in rotor based on the $2\times$ and $3\times$ super-harmonic frequency components and the crack-unbalance interactions. Commun. Nonlinear Sci. Numer. Simul. **13**, 2024–2040 (2008)
28. Darpe, A.K., Gupta, K., Chawla, A.: Transient response and breathing behaviour of a cracked Jeffcott rotor. J. Sound Vib. **272**, 207–243 (2004)
29. Papadopoulos, C.A.: The strain energy release approach for modelling cracks in rotors: a state of the art review. Mech. Syst. Signal Process. **22**, 763–789 (2008)
30. Wu, X., Sawicki, J.T., Friswell, M.I., Baaklini, G.Y.: Finite element analysis of coupled lateral and torsional vibrations of a rotor with multiple cracks. In: ASME Turbo Expo 2005: Power for Land, Sea, and Air, pp. 841–850. American Society of Mechanical Engineers (2005)
31. Darpe, A.K., Gupta, K., Chawla, A.: Coupled bending, longitudinal and torsional vibrations of a cracked rotor. J. Sound Vib. **269**, 33–60 (2004)
32. Papadopoulos, C.A.: Some comments on the calculation of the local flexibility of cracked shafts. J. Sound Vib. **278**, 1205–1211 (2004)
33. Bachschmid, N., Tanzi, E.: Deflections and strains in cracked shafts due to rotating loads: a numerical and experimental analysis. Int. J. Rotat. Mach. **10**, 283–291 (2004)
34. Penny, J.E.T., Friswell, M.I.: Simplified modelling of rotor cracks. Key Eng. Mater. **245–246**, 223–232 (2003). doi:10.4028/www.scientific.net/KEM.245-246.223
35. Green, I., Casey, C.: Crack detection in a rotor dynamic system by vibration monitoring—Part I: analysis. J. Eng. Gas Turbines Power **127**, 425–436 (2005)
36. Al-Shudeifat, M.A.: On the finite element modeling of the asymmetric cracked rotor. J. Sound Vib. **332**, 2795–2807 (2013)
37. Guo, C., Al-Shudeifat, M.A., Yan, J., Bergman, L.A., McFarland, D.M., Butcher, E.A.: Stability analysis for transverse breathing cracks in rotor systems. Eur. J. Mech. A Solids **42**, 27–34 (2013)
38. Jun, O.S., Gadala, M.S.: Dynamic behavior analysis of cracked rotor. J. Sound Vib. **309**, 210–245 (2008)
39. Al-Shudeifat, M.A., Butcher, E.A.: New breathing functions for the transverse breathing crack of the cracked rotor system: approach for critical and subcritical harmonic analysis. J. Sound Vib. **330**, 526–544 (2011)
40. Mayes, I., Davies, W.: Analysis of the response of a multi-rotor bearing system containing a transverse crack in a rotor. J. Vib. Acoust. Stress Reliab. Des. **106**, 139–145 (1984)
41. Sinou, J.J., Lees, A.W.: The influence of cracks in rotating shafts. J. Sound Vib. **285**, 1015–1037 (2005)
42. Al-Shudeifat, M.A., Butcher, E.A., Stern, C.R.: General harmonic balance solution of a cracked rotor-bearing-disk system for harmonic and sub-harmonic analysis: Analytical and experimental approach. Int. J. Eng. Sci. **48**, 921–935 (2010)
43. Darpe, A.K.: A novel way to detect transverse surface crack in a rotating shaft. J. Sound Vib. **305**, 151–171 (2007)
44. Pilkey, W.D.: Analysis and Design of Elastic Beams: Computational Methods. Wiley, New York (2002)
45. Sinou, J.J., Lees, A.W.: A nonlinear study of a cracked rotor. Eur. J. Mech. A Solids **26**, 152–170 (2007)
46. Cheng, L., Li, N., Chen, X.-F., He, Z.-J.: The influence of crack breathing and imbalance orientation angle on the characteristics of the critical speed of a cracked rotor. J. Sound Vib. **330**, 2031–2048 (2011)
47. Gasch, R.: A survey of the dynamic behaviour of a simple rotating shaft with a transverse crack. J. Sound Vib. **160**, 313–332 (1993)
48. Lees, A., Friswell, M.: The vibration signature of chordal cracks in asymmetric rotors. In: Proceedings of the 19th International Modal Analysis Conference, pp. 1–6 (2001)
49. Rubio, L., Muñoz-Abella, B., Rubio, P., Montero, L.: Quasi-static numerical study of the breathing mechanism of an elliptical crack in an unbalanced rotating shaft. Latin Am. J. Solids Struct. **11**, 2333–2350 (2014)
50. Staff, W.W.P.A.: Western Woods Use Book, 4th edn. Western Wood Products Association, Portland (1996)
51. Ishida, Y., Yamamoto, T.: Linear and Nonlinear Rotordynamics: A Modern Treatment with Applications, 2nd edn. Wiley, Weinheim (2013)